In vitro-in silico study on the influence of dose, fraction bioactivated and endpoint used on the relative potency value of pyrrolizidine alkaloid N-oxides compared to parent pyrrolizidine alkaloids

Yasser Alhejji [a,b,*,1], Frances Widjaja [a,*,1], Shenghan Tian [a], Thomas Hoekstra [a], Sebastiaan Wesseling [a], Ivonne M.C.M. Rietjens [a]

[a] *Division of Toxicology, Wageningen University, PO Box 8000, 6700 EA Wageningen, the Netherlands*
[b] *Department of Food Science and Human Nutrition, College of Agriculture and Veterinary Medicine, Qassim University, Buraydah 51452, Saudi Arabia*

ARTICLE INFO

ABSTRACT

Pyrrolizidine alkaloids (PAs) and their N-oxides (PA-N-oxides) are phytotoxins found in food, feed and the environment. Yet, limited data exist from which the relative potency of a PA-N-oxide relative to its corresponding PA (REP$_{PANO\ to\ PA}$) can be defined. This study aims to investigate the influence of dose, fraction bioactivated and endpoint on the REP$_{PANO\ to\ PA}$ of a series of pyrrolizidine N-oxides using in vitro-in silico data and physiologically based kinetic (PBK) modeling. The first endpoint used to calculate the REP$_{PANO\ to\ PA}$ was the ratio of the area under the concentration–time curve of PA resulting from an oral dose of PA-N-oxide divided by that from an equimolar dose of PA (Method 1). The second endpoint was the ratio of the amount of pyrrole-protein adducts formed under these conditions (Method 2). REP$_{PANO\ to\ PA}$ values appeared to decrease with increasing dose, with the decrease for Method 2 already starting at lower dose level than for Method 1. At dose levels as low as estimated daily human intakes, REP$_{PANO\ to\ PA}$ values amounted to 0.92, 0.81, 0.78, and 0.68 for retrorsine N-oxide, seneciphylline N-oxide, riddelliine N-oxide and senecivernine N-oxide, respectively, and became independent of the dose or fraction bioactivated, because no GSH depletion, saturation of PA clearance or PA-N-oxide reduction occurs. Overall, the results demonstrate the strength of using PBK modeling in defining REP$_{PANO\ to\ PA}$ values, thereby substantiating the use of the same approach for other PA-N-oxides for which in vivo data are lacking.

Introduction

Pyrrolizidine alkaloids (PAs) and their N-oxides (PA-N-oxides) are phytotoxins that can be found in food, feed and the environment. There are up to 1000 PAs and PA-N-oxides occurring in 3 % of global flowering plants (Stegelmeier et al., 1999; Smith and Culvenor, 1981), with PA-N-oxides occurring as the predominant form (Wuilloud et al., 2004; Yang et al., 2017). PA-N-oxides are generally assumed to be less toxic than their parent PAs because the N-oxides must first be reduced to their corresponding PAs by intestinal microbiota and liver cytochromes P450 (CYPs 450) (Mattocks, 1971; Yang et al., 2019; Tang et al., 2013). The PAs, upon bioactivation by CYPs P450 to reactive pyrrole intermediates, form adducts with proteins (Ruan et al., 2015; Ma et al., 2018; Chen et al., 2020; Ma et al., 2021) and DNA (Chou et al., 2003; He et al., 2017)

(Fig. 1) causing hepatotoxicity, genotoxicity and tumorigenicity. 1,2-Unsaturated PAs pose a chronic health risk upon long-term exposure resulting from for instance use of some herbal teas because they are considered to be genotoxic and carcinogenic, with MOE values that may be lower than 10,000 (Dusemund et al., 2018). Effects upon acute exposure to high dose levels include hepatic veno-occlusive disease (HVOD), liver cirrhosis and hepatic tumours, but the acute human health risk from short-term PA consumption is considered to be low based on an EFSA scientific risk assessment and other risk assessments (Dusemund et al., 2018; EFSA et al., 2017). Upon reduction and subsequent bioactivation, PA-N-oxides can cause the same adverse effects as their parent PAs (Yang et al., 2017; Chou et al., 2003; He et al., 2021).

Until now, limited data exist from which the relative potency of a PA-N-oxide compared to its corresponding PA ($REP_{PANO \ to \ PA}$) can be defined (Fig. 1). In vitro studies generally provide inadequate $REP_{PANO \ to \ PA}$ values since the reduction of the PA-N-oxide to the corresponding PA by intestinal microbiota is generally not taken into account, resulting in $REP_{PANO \ to \ PA}$ values < 0.1 (He et al., 2017; Allemang et al., 2018; Louisse et al., 2019). In addition, assuming the PA-N-oxides to be equally potent as their parent PA ($REP_{PANO \ to \ PA}$ value equals 1.0 (Merz and Schrenk, 2016) may overestimate the risk given that the reduction of the PA-N-oxide may be incomplete or may result in a lower area under the concentration time curve (AUC) for the parent PA with a lower maximum plasma concentration (C_{max}) than what is observed upon dosing the PA itself (Yang et al., 2017; Yang et al., 2019).

Some in vivo data exist for a selected number of PAs and PA-N-oxides from which $REP_{PANO \ to \ PA}$ values can be derived that take into account the in vivo PA-N-oxide kinetics. Table 1 provides such data available for
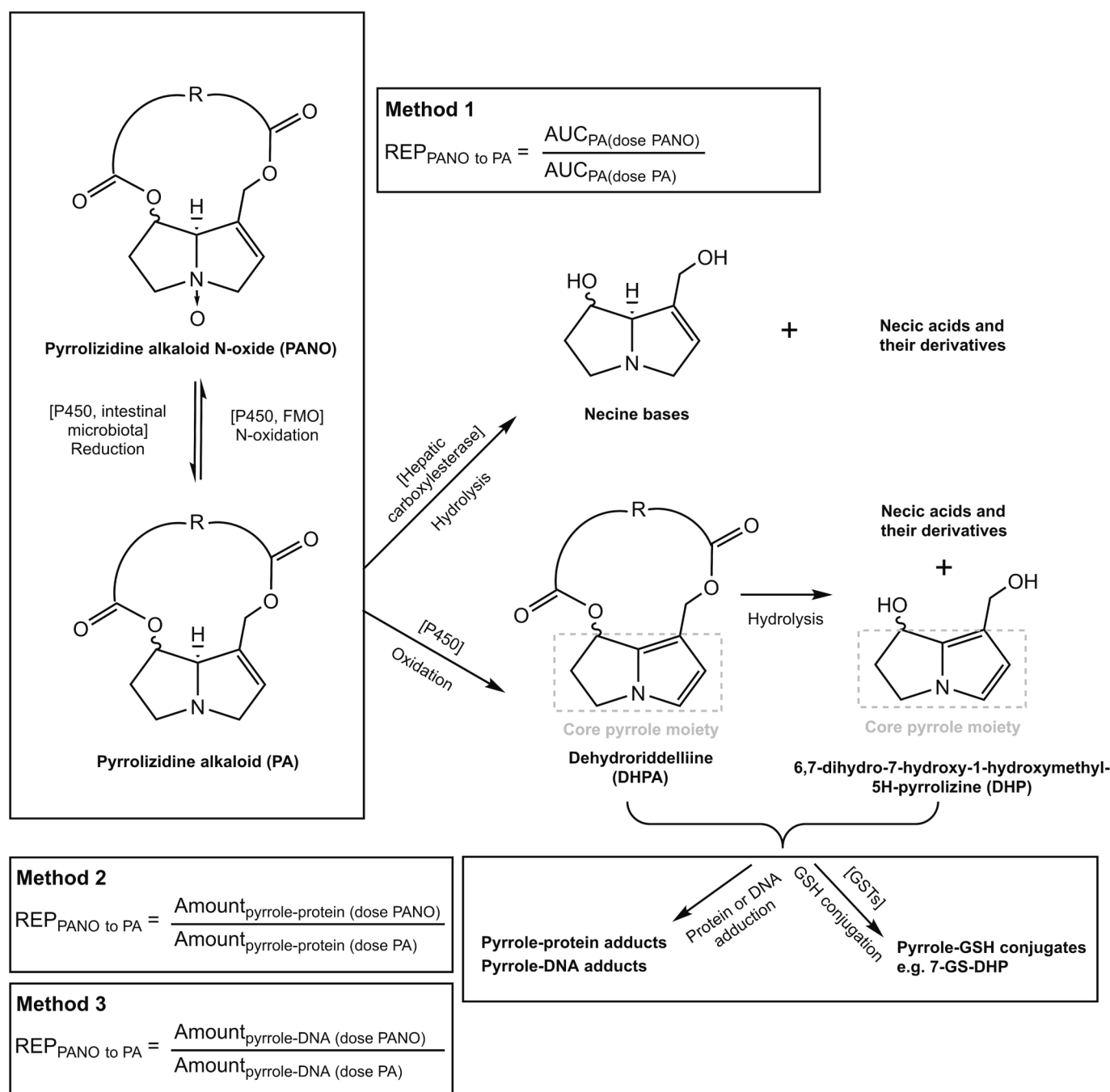

Fig. 1. Metabolic pathways for PA-N-oxides and PAs, and the three methods for determining the $REP_{PANO \ to \ PA}$ value.

Table 1

In vivo $REP_{PANO\ to\ PA}$ values of RIDO relative to RID calculated at different dose levels and endpoints in rats. Further details on the 3 methods to calculate the $REP_{PANO\ to\ PA}$ value are presented in Fig. 1. BW is abbreviation for body weight.

Dose (µmol·kg⁻¹ BW)	Duration	Oral RIDO administration	Oral RID administration	$REP_{PANO\ to\ PA}$	Reference
Parameter quantified					
AUC of RID (µg·min mL⁻¹) (Method 1 Fig. 1)					
28.62	Single dose	–	30.96 ± 4.80	0.32[a]	Williams et al. (Williams et al., 2002)
54.74	Single dose	19.22 ± 6.99	–		Yang et al. (Yang et al., 2019)
Amount of pyrrole-protein adducts (ng·g⁻¹ protein) (Method 2 Fig. 1)					
4.5	3 Daily doses	295.00 ± 33.10	348.00 ± 31.20	0.85	Xia et al. (Xia et al., 2016)
24	3 Daily doses	707.00 ± 62.90	1197.00 ± 216.00	0.59	Xia et al. (Xia et al., 2016)
Amount of pyrrole-DNA adducts (adducts·10⁻⁸ nucleotides) (Method 3 Fig. 1)					
24	3 Daily doses	8.47	13.2	0.64	Xia et al. (Xia et al., 2013)
2.9	Single dose	–	1180	0.36[a,b]	Wang et al. (Wang et al., 2005)
2.7	Single dose	399	–		Wang et al. (Wang et al., 2005)

[a]Dose normalized $REP_{PANO\ to\ PA}$ value = (AUC RID from oral RIDO / dose of RIDO) / (AUC RID from oral RID / dose of RID).

[b]Quantification of DNA adduct levels by ^{32}P-post-labelling may be less accurate than by LC-MS/MS.

riddelliine N-oxide (RIDO) and riddelliine (RID). To estimate $REP_{PANO\ to\ PA}$ values, the PA and its N-oxide should preferably be dosed in the same study at equimolar levels characterizing the same endpoint. Table 1 reveals that such data sets exist for the amount of pyrrole-protein adducts and the amount of pyrrole-DNA adducts formed, in studies with RIDO and RID reported by Xia et al. (Xia et al., 2016; Xia et al., 2013). From these data a $REP_{PANO\ to\ PA}$ value for RIDO relative to RID can be derived that is lower than 1.0 and also appears to be lower at a higher dose level (Table 1).

The data presented in Table 1, also reveal that calculating the $REP_{PANO\ to\ PA}$ value based on the AUC for the parent PA RID can only be achieved using data from two different studies administering orally either only RID (Williams et al., 2002) or only RIDO (Yang et al., 2019) at different single dose levels. After dose-normalization, the AUC of RID from oral RIDO divided by that from oral RID yielded a REP value of 0.32. This $REP_{PANO\ to\ PA}$ value might be unreliable because the two studies did not only use different dose levels, but they also used different rat strains, with Williams et al. using Fisher rats (Williams et al., 2002) and Yang et al. using Sprague-Dawley rats (Yang et al., 2019). In addition, Williams et al. (Williams et al., 2002) fed the rats ad libitum, while Yang et al. (Yang et al., 2019) only stated the administration of distilled water before compound administration.

Fig. 1 presents the metabolic scheme for PA-N-oxides and PAs including the bioactivation to the reactive pyrrole intermediates such as 6,7-dihydro-7-hydroxy-1-hydroxymethyl-5H-pyrrolizine (DHP) and dehydroretronecine (DHR). The figure also presents the different endpoints used in Table 1 for calculating the $REP_{PANO\ to\ PA}$ value. In a previous study (Widjaja et al., 2022), it was shown that when based on the AUC for the parent PA the $REP_{PANO\ to\ PA}$ value may decrease with the dose because of saturation of PA clearance and saturation of PA-N-oxide reduction. The reason for a reduction in the $REP_{PANO\ to\ PA}$ value of RIDO compared to RID when based on the amount of pyrrole-protein or pyrrole-DNA adducts, as observed in vivo (Table 1) remains to be elucidated. The overview in Fig. 1 illustrates that the reactive pyrrole intermediates could either be conjugated with glutathione (GSH) forming 7-glutathione-DHP (7-GS-DHP) as the major conjugate (Tamta et al., 2012; Ning et al., 2019), or react with protein and DNA forming pyrrole-protein and pyrrole-DNA adducts. This competition for pyrrole scavenging by GSH on the one hand or by protein and DNA on the other hand may result in an effect on the $REP_{PANO\ to\ PA}$ value when the kinetics for GSH conjugation would vary with the dose between the PA and the PA-N-oxide. This could explain an influence of the dose on the $REP_{PANO\ to\ PA}$ value when calculated based on pyrrole-protein or DNA adducts. The physiologically based kinetic (PBK) modeling allows for studying such a hypothesis without the need for experiments with large numbers of experimental animals. At the same time it provides a new approach methodology (NAM) where, in contrast to the in vitro studies reported so far (He et al., 2017; Allemang et al., 2018; Louisse et al., 2019), the role of PA-N-oxide reduction by liver and especially intestinal microbiota can

be included.

The aims of the present study were to: 1) generate more insight into the influence of dose, fraction bioactivated and endpoint used on the relative potency value of RIDO compared to RID using PBK modeling as a novel testing strategy, and 2) extend the approach to other pairs of PA-N-oxides and PAs including seneciphylline N-oxide (SNPO), retrorsine N-oxide (RTRO), senecivernine N-oxide (SVRO) and their corresponding parent PAs (Fig. 2). In our previous study, this in vitro - in silico approach provided insight in the $REP_{PANO\ to\ PA}$ value of senecionine N-oxide (SENO) relative to senecionine (SEN) (Widjaja et al., 2023). Studying it for another PA-N-oxide and its PA for which in vivo data to define a REP value are available (RIDO and RID) will reveal whether the approach might be applied to PA-N-oxides and PAs for which in vivo data are lacking (SNPO, RTRO, SVRO and their PAs). At the same time building the PBK models for additional PAs for which in vivo data on blood concentrations are available for PBK model evaluation, will further validate the PBK models and support their use for prediction of the $REP_{PANO\ to\ PA}$ values. All PA-N-oxides selected for the present study are of macrocyclic diester configuration for the purpose of direct comparison.

Materials and methods

Materials

Riddelliine (RID, 99 %), seneciphylline N-oxide (SNPO, 98 %), seneciphylline (SNP, 99 %), retrorsine N-oxide (RTRO, 96 %), retrorsine (RTR, 99 %), senecivernine N-oxide (SVRO, 98 %) and senecivernine (SVR, 99 %) were purchased from Phytolab (Phytolab GmbH & Co. KG, Germany) and were prepared in DMSO purchased from Acros Organics (Geel, Belgium). Acetonitrile (ACN, UPLC/MS grade) was purchased from Biosolve (Valkenswaard, the Netherlands). Di-potassium hydrogen phosphate trihydrate ($K_2HPO_4 \cdot 3H_2O$) and potassium dihydrogen phosphate (KH_2PO_4) were purchased from Merck (Amsterdam, the Netherlands). The reduced form of nicotinamide adenine dinucleotide phosphate (NADPH) was purchased from Carbosynth (Carbosynth, UK). L-glutathione-reduced form (GSH, purity ≥ 98 %) was purchased from Sigma-Aldrich, now rebranded as Merck (Amsterdam, the Netherlands). Pooled rat liver S9 from male Sprague-Dawley (SD) rats was purchased from Corning (Amsterdam, the Netherlands). Phosphate-buffered saline (PBS, pH 7.4) was purchased from Gibco (Paisley, USA). Fresh rat fecal samples from Wistar rats (10 males and 10 females) were a gift from BASF (Ludwigshafen, Germany) and were collected, treated, and stored as previously described (Widjaja et al., 2022). Rat fecal samples were collected fresh immediately after feces excretion. Rat liver S9 samples were purchased from industries, all already possessing the license to provide these materials for research purposes.
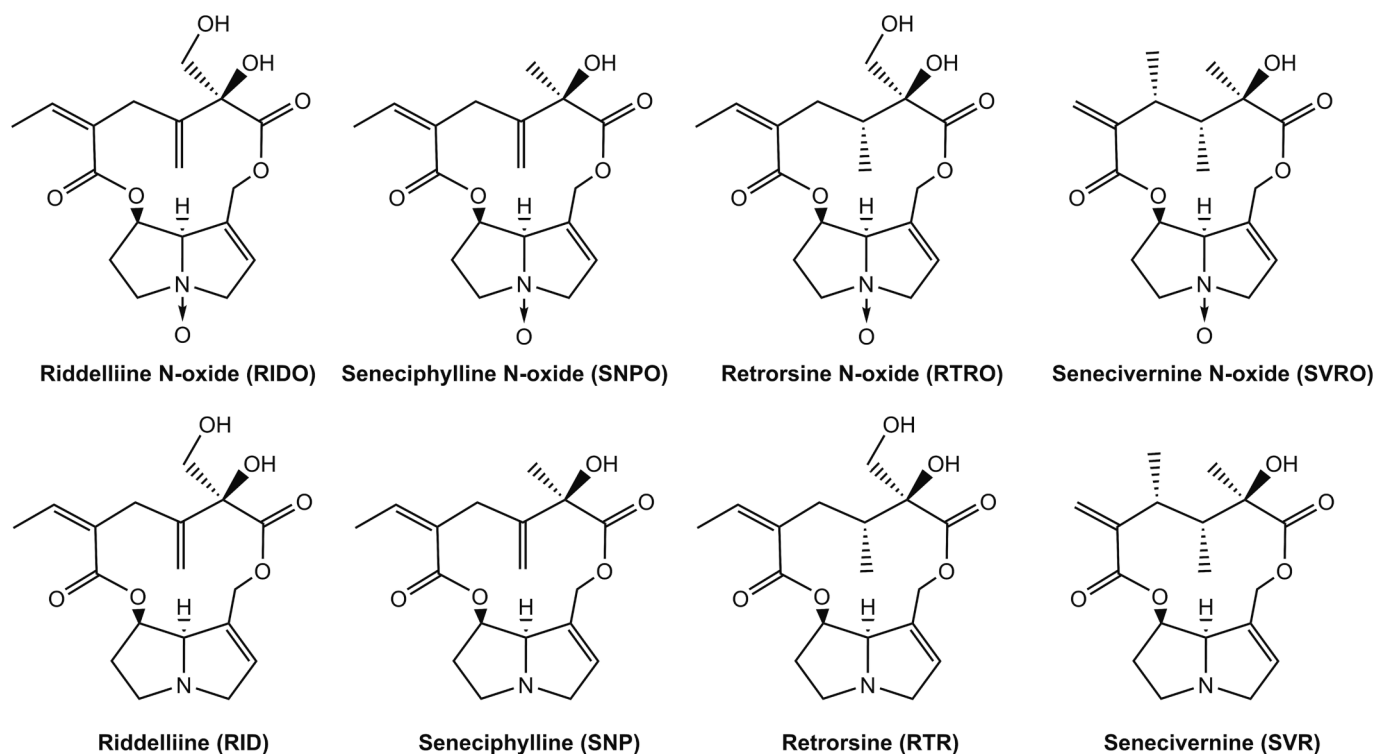
Fig. 2. Chemical structures of the studied PA-N-oxides and their corresponding parent PAs.

In vitro incubations to derive kinetic constants

In vitro incubations were conducted to obtain kinetic constants (V_{max}, K_m and k_{cat}) as input for the PBK models. The reduction of SNPO, RTRO and SVRO to the corresponding parent PAs by intestinal microbiota and liver was studied as described in previous studies with RIDO (Widjaja et al., 2022) and SENO (Ning et al., 2019; Ning et al., 2019) using anerobic incubations with rat feces and aerobic incubations with rat liver S9. The clearance of SNP, RTR and SVR was investigated using aerobic incubations with rat liver S9 following a procedure similar to the one described for RID (Widjaja et al., 2022) and SEN (Ning et al., 2019; Ning et al., 2019). 7-GS-DHP formation from SNP, RTR and SVR and RID was determined using aerobic incubations with rat liver S9 in the presence of GSH as previously performed for SEN (Widjaja et al., 2023). The optimal conditions employed to study the reduction of PA-N-oxides to the free base PAs, the clearance of parent PAs and the formation of 7-GS-DHP are summarized in Table 2. At these conditions, product formation was shown to be linear in time and with the amount of protein.

LC-MS/MS analysis of PAs

The reduction of the PA-N-oxides and the clearance of their parent PAs were quantified using liquid chromatography with tandem mass spectrometry (LC-MS/MS). The analysis was performed using a UHPLC system (Shimadzu SIL-40C XR autosampler) coupled with a column oven (Shimadzu CTO-40C) and a valve unit (Shimadzu FCV-20AH2) combined with an MS system (Shimadzu LCMS-8045, Kyoto, Japan). A 1 μL injection volume of sample was examined with a reverse phase C18 column (Phenomenex 1.7 μm 2.1 × 50 mm) at a flow rate of 0.3 mL/min. Milli-Q water and acetonitrile were used as mobile phases, each containing 0.1 % v/v formic acid. The measurement started with 0 % to 100 % ACN for 6 min. 100 % ACN was kept for 1 min after which it changed to the starting condition of 0 % ACN within 1 min. Prior to the next injection, this percentage was kept for 4 min. The PAs and their PA-N-oxides were analyzed with a positive ionizing mode and quantified in the multiple reaction monitoring (MRM) mode; detailed information on $[M + H]^+$ of precursors to products *m/z*, collision energy (CE) and retention times (RT) can be found in Table 1S of the Supplementary Material. Calibration curves of these compounds were defined using commercially available reference compounds in a range of 0.001–1 μM, and employed to quantify the concentrations of PAs in the samples using the total ion chromatogram (TIC).

Table 2
Optimized incubation conditions for obtaining kinetic constants for metabolism of PA-N-oxides and their parent PAs.

Compound	Reduction of PA-N-oxides with rat feces		Reduction of PA-N-oxides with rat liver S9		Clearance of parent PAs with rat liver S9		Incubation of parent PAs with rat liver S9 to form 7-GS-DHP	
	Feces (g feces mL^{-1})	Time (min)	S9 protein (mg mL^{-1})	Time (min)	S9 protein (mg mL^{-1})	Time (min)	S9 protein (mg mL^{-1})	Time (min)
SNPO	0.06	180	1.0	60	–	–	–	–
SNP	–	–	–	–	1.0	60	1.0	60
RTRO	0.04	120	1.0	60	–	–	–	–
RTR	–	–	–	–	0.5	60	1.0	60
SVRO	0.04	120	1.0	60	–	–	–	–
SVR	–	–	–	–	0.5	30	1.0	60
RID	–	–	–	–	–	–	1.0	60

LC-MS/MS analysis of 7-GS-DHP

7-GS-DHP was quantified by LC-MS/MS using a Shimadzu Nexera XR LC-20AD XR UHPLC system coupled with a Shimadzu LCMS-8040 MS (Kyoto, Japan). A 1 μL aliquot was loaded onto a reverse phase C18 column (Phenomenex 1.7 μm 2.1 x 50 mm). The flow rate was 0.3 mL/min and the mobile phase was made with ultrapure water with 0.1 % (v/v) formic acid and ACN containing 0.1 % (v/v) formic acid. The mobile phase was composed of water and ACN. A linear gradient was applied from 0 to 5 % ACN in 8 min and was further increased to 100 % ACN in 6 min. This percentage was kept for 0.5 min and was then reduced to the starting conditions in 0.1 min. The column was equilibrated for another 4 min at the starting conditions before the next injection, and detailed information on $[M + H]^+$ of precursors to products *m/z*, collision energy (CE) and retention times (RT) can be found in Table 1S of the Supplementary Material. Quantification was done by comparing the peak area of the 7-GS-DHP formed in the incubation samples to the calibration curve of 7-GS-DHP ranging from 0.078 to 10 μM ($r^2 = 0.991$) previously reported by Ning et al. using the same conditions and LC-MS/MS instrument (Ning et al., 2019; Ning et al., 2019).

Determination of kinetic constants

Kinetic constants were obtained from PA-N-oxide concentration-dependent rates for PA-N-oxide reduction or PA concentration-dependent rates for PA clearance and 7-GS-DHP formation as previously described for RIDO (Widjaja et al., 2022) and SENO (Widjaja et al., 2023). The amount of PA formed was determined as the amount detected in full incubations minus the amount detected in the blanks (without feces or NADPH), while the amount of PA cleared was determined as the amount detected in blanks (without NADPH) minus the amount in the full incubations. The amount of 7-GS-DHP formed was determined as the amount detected in full incubations minus the amount detected in the blanks (without NADPH). Kinetic constants for PA-N-oxide reduction by intestinal microbiota and rat liver S9, PA clearance and 7-GS-DHP formation from PAs were determined by fitting the data using GraphPad (GraphPad Prism Software version 10.0.2, San Diego, CA, USA).

Kinetic constants for PA formation from PA-N-oxides in incubations with rat feces, PA clearance and 7-GS-DHP formation from PAs in incubations with rat liver samples, were obtained by fitting the data to the Michaelis-Menten equation:

$$v = \frac{V_{max}}{1 + \frac{K_m}{[S]}} = \frac{V_{max} \times [S]}{K_m + [S]}$$

where *v* is the rate of reaction (μmol·h^{-1}·g·feces^{-1} or nmol·min^{-1}·mg^{-1}·S9 protein), V_{max} the maximum rate of reaction (μmol·h^{-1}·g·feces^{-1} or nmol·min^{-1}·mg^{-1}·S9 protein), K_m the Michaelis–Menten constant (μM), and *[S]* the substrate concentration (μM). V_{max} was scaled to an in vivo value (L·h^{-1}) by either: 1) using a fecal fraction to body weight (fbw) of 0.0164 g rat feces·g^{-1} BW (Wang et al., 2020; Mendez-Catala et al., 2021; Hoskins and Zamcheck, 1968) based on a defecation volume per day of 4.1 g and a body weight (BW) of 0.25 kg, or 2) using an S9 protein yield of 143 mg S9 protein·g^{-1} rat liver, a rat liver weight of 34 g·kg^{-1} BW and a BW of 0.25 kg (Punt et al., 2008). To mimic the effect of internal GSH depletion the V_{max} for 7-GS-DHP formation was multiplied by a % to define the residual V_{max}, to describe the accompanying reduction in the overall rate of 7-GS-DHP formation.

Since PA formation from PA-N-oxides in incubations with rat liver S9 appeared to follow first-order reaction kinetics, the slope of the plot for the formation rate versus substrate concentration directly represents k_{cat}, which equals V_{max} / K_m, but does not define V_{max} and K_m values as such. This can be derived from the Michaelis-Menten equation for substrate concentrations at *[S]* ≪ K_m, where $1 + K_m / [S]$ equals $K_m / [S]$.

Consequently, the Michaelis-Menten curve in the range where *[S]* ≪ K_m becomes:

$$v = \frac{V_{max}}{1 + \frac{K_m}{[S]}} = \frac{V_{max}}{\frac{K_m}{[S]}} = \frac{V_{max}}{K_m}[S] = k_{cat}[S]$$

where *v* is the rate of reaction (nmol·min^{-1}·mg^{-1}·protein), V_{max} the apparent maximum rate of reaction (nmol·min^{-1}·mg^{-1}·protein), K_m the apparent Michaelis-Menten constant (μM), and *[S]* the substrate concentration (μM). The slope k_{cat} was determined by fitting the data to the linear regression model. The in vitro k_{cat} expressed in mL·min^{-1}·mg^{-1} S9 protein thus obtained was scaled to an in vivo value expressed in L·h^{-1} by using an S9 protein yield of 143 mg S9 protein ·g^{-1} rat liver, a rat liver weight of 34 g·kg^{-1} BW and a BW of 0.25 kg (Punt et al., 2008).

Building the PBK model

The PBK model for PA-N-oxides with a submodel for PAs in rats (Fig. 3) previously developed and evaluated for RID (Widjaja et al., 2022) was extended to include GSH-scavenging of the reactive pyrrole intermediate through 7-GS-DHP formation from PAs (Ning et al., 2019; Widjaja et al., 2023), with 7-GS-DHP being the major metabolite formed in this reaction. Rat liver S9 incubations were used to derive kinetic constants for 7-GS-DHP formation and to build the rat model because rat data for RID were available from which REP$_{PANO\ to\ PA}$ values for validation of the approach could be performed for RIDO before extending the model to other PA-N-oxides. The Supplementary Material presents the model code in which changes in the model code highlighted in red indicate changes in the model as compared to the model code reported before (Widjaja et al., 2022) in order to include the 7-GS-DHP formation. The apparent permeability coefficient (P$_{app}$) values to derive absorption constant for all PAs and PA-N-oxides, and the other physiological, physicochemical, and kinetic parameters can also be found in the Supplementary Material. For SNP and RTR and their corresponding PANOs, the bioavailability was based on fitting the PBK model predictions to available in vivo data resulting in values of 10 % and 24 %, respectively (see Result section for details). For SVRO and SVR, an F (oral bioavailability) of 15 % reported for RIDO and RID (Widjaja et al., 2022) was used as there are no available in vivo data that define the bioavailability of SVRO and SVR. Additionally, it is important to note that the N-oxidation of the PAs to their PA-N-oxides is included in the general clearance of the PAs, while its contribution to the overall amount of PA-N-oxide upon dosing the PA-N-oxide is considered negligible. The model was built in Berkeley Madonna version 9.1.18 and was run with the Rosenbrock (stiff) method as ordinary differential equations solver.

To include 7-GS-DHP formation, the equation in the PA submodel for the change in the amount of PA in the liver was extended to read as follows with RID as example:

AL$_{RID}$'=QL*(CB$_{RID}$–CVL$_{RID}$)+kb1*ASI$_{RID}$+kb2*ALI$_{RID}$+ALM1'-ALM2'-ALM3'+ALM3'

where AL$_{RID}$' is the change in the total amount of RID in liver tissue, QL* (CB$_{RID}$ – CVL$_{RID}$) is the net amount of RID going into the liver from RID that enters from arterial blood and leaves to the systemic blood circulation, k_{b1}*ASI$_{RID}$ is the amount of RID entering the liver via the portal vein from the small intestine, and k_{b2} * ALI$_{RID}$ reflects the uptake of RID from the large intestine where it is formed from RIDO via reduction by gut microbiota, ALM1' is the amount of RID formed by RIDO reduction in the liver, and ALM2' is the amount of RID metabolized or cleared in the liver. This part of the equation is similar to what was previously included in the model code. The term ALM3' reflects the formation of 7-GS-DHP from RID. Given that this conversion described by the term -ALM3' was also included in the overall clearance of RID (described by the term - ALM2'), also a term + ALM3' was added to the equation to avoid that this part of the clearance is subtracted twice when modeling the change in the amount of RID in the liver. Subtracting and adding the
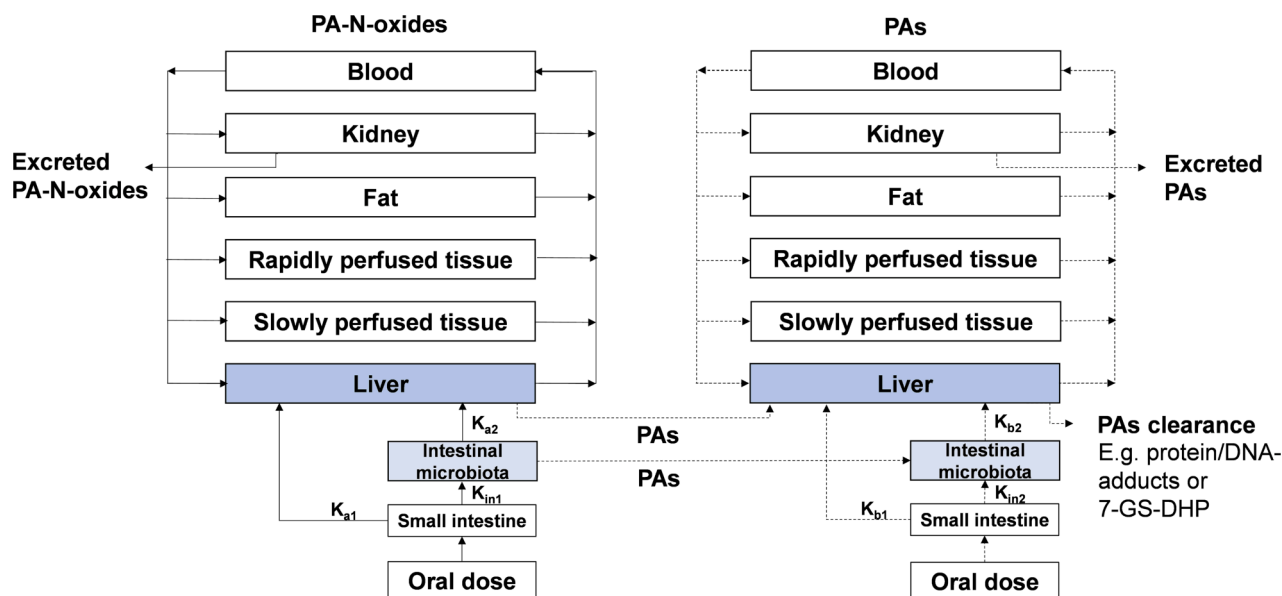
Fig. 3. PBK model for PA-N-oxides with a submodel for PAs as adapted from Widjaja et al. (Widjaja et al., 2022) with the addition of 7-GS-DHP formation to enable calculation of pyrrole-protein adduct formation.

reaction that forms 7-GS-DHP from the entire RID clearance (- ALM3′ + ALM3′) allows quantification of 7-GS-DHP formation without disturbing the mass balance of this model (Ning et al., 2019; Widjaja et al., 2023; Ning et al., 2019).

Methods to calculate the REP$_{PANO\ to\ PA}$ value

In line with the available in vivo data from which REP$_{PANO\ to\ PA}$ values can be derived (Table 1), the present work used three methods to calculate the REP$_{PANO\ to\ PA}$ values (Fig. 1) as presented in the equations below:

Method 1

$$REP_{PANO\ to\ PA} = \frac{AUC_{PA\ (dose\ PANO)}}{AUC_{PA\ (dose\ PA)}}$$

Method 2

$$REP_{PANO\ to\ PA} = \frac{Amount_{pyrrole-protein\ adducts\ (dose\ PANO)}}{Amount_{pyrrole-protein\ adducts\ (dose\ PA)}}$$

Method 3

$$REP_{PANO\ to\ PA} = \frac{Amount_{pyrrole-DNA\ adducts\ (dose\ PANO)}}{Amount_{pyrrole-DNA\ adducts\ (dose\ PA)}}$$

Method 1 has been used in our previous work on RID and its N-oxide (Widjaja et al., 2022), while Method 2 and 3 allow calculation of the REP$_{PANO\ to\ PA}$ value based on other endpoints. Method 2 and 3 both allow for consideration of the effect of reduction in GSH scavenging of the pyrrole intermediate potentially resulting in relatively higher levels of DHP to react to either protein or DNA adducts when GSH scavenging would be saturated or limited by reduction in levels of GSH (Fig. 1). The amount of pyrrole-protein adducts and pyrrole-DNA adducts formed are known to be correlated (Zhu et al., 2022), although, as also shown by the data in Table 1, the amount of pyrrole-DNA adducts may be only a small fraction of the amount of pyrrole-protein adducts formed (Zhu et al., 2022). Given that the amount of pyrrole-DNA adducts may amount to

only a fraction of the amount of pyrrole-protein adducts, in the modeling its influence on the amount of pyrrole-protein adducts was considered negligible. Therefore, the REP$_{PANO\ to\ PA}$ value from Method 2 and Method 3 are assumed to be similar, and only REP$_{PANO\ to\ PA}$ values from Method 2 will be simulated by PBK modeling in this present work.

Furthermore, since the total amount of pyrrole-protein adducts can be expected to vary not only with the dose but also with the fraction of the dose bioactivated to reactive pyrrole intermediates, the modeling also included a value f representing the fraction of the dose bioactivated. As a result, the REP$_{PANO\ to\ PA}$ value defined by Method 2 can be described by the following equation:

$REP_{PANO\ to\ PA}\ Method\ 2$

$$= \frac{Amount_{pyrrole-protein\ adducts\ (PANO)}}{Amount_{pyrrole-protein\ adducts\ (PA)}}$$
$$= \frac{F\ \times\ REP_{PANO\ to\ PA}\ Method\ 1\ \times\ f\ \times\ Dose_{PANO} - Amount_{7-GS-DHP\ (PANO)}}{F\ \times\ f\ \times\ Dose_{PA}\ -\ Amount_{7-GS-DHP\ (PA)}\ \times\ \%residual\ V_{max}}$$

In which *amount*$_{pyrrole-protein\ adducts\ (PANO)}$ (μmol) is the amount of pyrrole-protein adducts formed upon oral PANO administration, *amount*$_{pyrrole-protein\ adducts\ (PA)}$ (μmol) is the amount of pyrrole-protein adducts formed upon oral PA administration, F is the oral bioavailability of PANO and PA that has for RID previously been estimated at 15 % (Widjaja et al., 2022); $REP_{PANO\ to\ PA}\ Method\ 1$ is the REP$_{PANO\ to\ PA}$ value derived from the ratio of the AUC of PA from oral PANO administration divided by the AUC of PA from oral PA administration, f is the fraction of the dose bioactivated to active pyrrole intermediates, $dose_{PANO}$ is the oral dose of administered PANO (μmol), $dose_{PA}$ is the equimolar dose of administered PA (μmol), *amount*$_{7-GS-DHP\ (PANO)}$ (μmol) is the amount of 7-GS-DHP at 24 h from oral PANO administration, *amount*$_{7-GS-DHP\ (PA)}$ (μmol) is the amount of 7-GS-DHP at 24 h from oral PA administration, and $\%residual\ V_{max}$ is the factor applied to describe the effect of GSH depletion and hence the reduction in the rate of 7-GS-DHP formation upon increasing dose of oral PA.

At low dose levels, the bioavailability or fraction bioactivated no longer influence the REP$_{PANO\ to\ PA}$ value outcome (see Result section). Thus, for the purpose of comparison, the REP$_{PANO\ to\ PA}$ values were calculated using the same input parameters as for RID for the 3 additional PA-N-oxides. This included a % residual V_{max} of 87 % at high dose level of 24 μmol·kg^{-1} BW, an f of 0.40 and compound specific

bioavailability data of 10 % for SNPO, 24 % for RTRO and 15 % for SVRO.

Sensitivity analysis

A sensitivity analysis was performed to assess which parameters of the PBK model have the largest impact on the predicted $amount_{pyrrole-protein\ adducts}$, which is the parameter for calculating the $REP_{PANO\ to\ PA}$ by Method 2. A sensitivity analysis for the AUC of PA, which was the parameter used for calculating the $REP_{PANO\ to\ PA}$ by Method 1, was previously presented (Widjaja et al., 2022) and appeared to be unaffected by including pyrrole-GSH (i.e. 7-GS-DHP) and pyrrole-protein adducts formation in the model. Normalized SCs were calculated using the equation below:

$$SC = \frac{(C' - C)/C}{(P' - P)/P}$$

where C is the initial value of the model output, C' is the modified value of the model output with a 5 % increase of an input parameter, P is the initial parameter value, and P' is the parameter value with an increase of 5 %. Only one parameter was changed each time, while the other parameters were kept at their initial values. A large SC value indicates that the respective parameter has a large impact on the predicted $amount_{pyrrole-protein\ adducts}$.

Results

RIDO and RID

7-GS-DHP formation from RID

The rate of formation of 7-GS-DHP in rat liver S9 incubations with increasing concentrations of RID is shown in Fig. 4. The results obtained reveal Michaelis-Menten kinetics resulting in the V_{max} and K_m values presented in Table 3. V_{max} and K_m values were used as input for the PBK model to describe the in vivo RID concentration dependent formation of 7-GS-DHP from either an oral dose of RIDO or RID. Since at dose levels of 24 μmol·kg^{-1} BW, the dose level of RIDO used in the in vivo rat study of Xia et al. (Xia et al., 2016), and an equimolar dose of RID, the maximum concentrations of RID in the liver were predicted by the PBK model to be 0.21 μM and 0.49 μM, respectively, it can be concluded that the RID concentrations in the liver will be substantially (387- and 166-fold) lower than the K_m for 7-GS-DHP formation determined to be 81.2 μM (Table 3). This implies that limitations in 7-GS-DHP formation are unlikely to result from saturation of the underlying kinetics. Thus, it was concluded that at high dose RID, limitation of the GSH pyrrole-
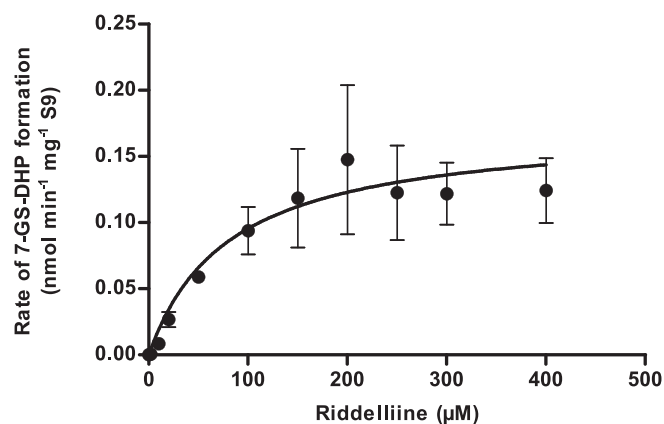

Fig. 4. RID concentration dependent rate of 7-GS-DHP formation in aerobic rat liver S9 incubations. Data are presented as mean ± SD of three independent experiments (n = 3).

Table 3
Kinetic constant for 7-GS-DHP formation from RID by rat liver S9 as derived from the data in Fig. 4. The parameters $V_{max,\ in\ vivo}$ and K_m are used in the PBK model simulations, where $V_{max,\ in\ vivo}$ can be decreased by multiplying with a percentage residual V_{max} to mimic the effect of GSH depletion and the resulting reduction in 7-GS-DHP formation.

Parameters	Value
$V_{max,\ in\ vitro}$ [nmol·min^{-1}·mg^{-1} S9 protein]	0.17
$V_{max,\ in\ vivo}$ [μmol·h^{-1}][a]	12.4
K_m [μM]	81.2
$k_{cat,\ in\ vitro}$ [mL·min^{-1}·mg^{-1} S9 protein][b]	0.0021
$k_{cat,\ in\ vivo}$ [L·h^{-1}][c]	0.1527

[a] $V_{max,\ in\ vivo}$ = [($V_{max,\ in\ vitro}$) / 1000] × 60 × [S9 in liver] × [liver weight] × BW. Rat S9 is 143 mg S9 protein ·g^{-1} liver, the weight of rat liver is 34 g·kg^{-1} BW and rat body weight is 0.25 kg; [b] $k_{cat,\ in\ vitro}$ = ($V_{max,\ in\ vitro}$) / K_m; [c] $k_{cat,\ in\ vivo}$ = ($V_{max,\ in\ vivo}$) / K_m.

scavenging capacity may result from internal GSH depletion rather than from saturating enzyme kinetics.

PBK modeling simulation for RIDO and RID

After incorporating the kinetic constants for 7-GS-DHP formation in the PBK model, the model was used to calculate the $REP_{PANO\ to\ PA}$ values of RIDO relative to RID for the two endpoints used in Method 1 and 2. This was done at i) an equimolar dose level of either 4.5 μmol·kg^{-1} BW or 24 μmol·kg^{-1} BW of RIDO and RID, the dose levels used in the reported in vivo rat studies of Xia et al. (Xia et al., 2016), ii) assuming a bioavailability of 15 % since that was reported before to result in PBK model predictions that best match the available in vivo kinetic data for RID (Widjaja et al., 2022), and iii) for different values of the percentage residual V_{max} for 7-GS-DHP adduct formation. The latter was done to mimic the consequences of GSH depletion and to determine at which value for the residual V_{max} the $REP_{PANO\ to\ PA}$ value obtained best matches the $REP_{PANO\ to\ PA}$ value calculated by Method 2 from the in vivo data available for RIDO and RID (Table 1).

Fig. 5 shows the results obtained when the fraction of the initial dose that is bioactivated into pyrrole intermediates is set at 0.40 (40 %). The results obtained reveal that under these conditions, the $REP_{PANO\ to\ PA}$ value calculated by Method 2 decreases upon increasing level of GSH depletion with a concomitant reduction in residual V_{max} upon dosing RID. In addition, with increasing depletion of GSH and thus further reduction of the V_{max} value for 7-GS-DHP adduct formation upon dosing RID, the discrepancy between the $REP_{PANO\ to\ PA}$ values from Method 1 and 2 becomes more pronounced. When the predicted $REP_{PANO\ to\ PA}$ values were compared with the values derived from the in vivo data (Table 1), Fig. 5a shows that the $REP_{PANO\ to\ PA}$ value obtained by Method 2 (0.78) closely matches the in vivo value (0.85) at 4.5 μmol·kg^{-1} BW with 100 % residual V_{max} when dosing RID, signifying no GSH depletion at this condition. On the other hand, Fig. 5b shows that the $REP_{PANO\ to\ PA}$ value obtained by Method 2 exactly matches the in vivo value (amounting to 0.59) at 24 μmol·kg^{-1} BW with 87 % residual V_{max} when dosing RID. The $REP_{PANO\ to\ PA}$ value obtained by Method 3 of 0.64, which is also presented in Fig. 5, is also comparable to the value of 0.59 obtained by Method 2, and thus also in line with the predictions obtained at 87 % residual V_{max} when dosing RID.

Using the results thus obtained for the % residual V_{max} values, Fig. 6 presents the dose dependent effect on the $REP_{PANO\ to\ PA}$ value as determined by Method 1 and 2. To simulate these effects, the % residual V_{max} in case of Method 2 was gradually decreased from 100 % at a dose of 4.5 μmol·kg^{-1} BW to the value of 87 % at a dose level of 24 μmol·kg^{-1} BW, and further decreased in the same linear way at dose levels above 24 μmol·kg^{-1} BW. The results show that for both Method 1 and Method 2, the $REP_{PANO\ to\ PA}$ value of 0.78 at 4.5 μmol·kg^{-1} BW decreases with increasing dose level reaching 0.70 (Method 1) and 0.19 (Method 2) at 154 μmol·kg^{-1} BW, with the reduction in the $REP_{PANO\ to\ PA}$ value determined by Method 1 starting to occur from a higher dose level

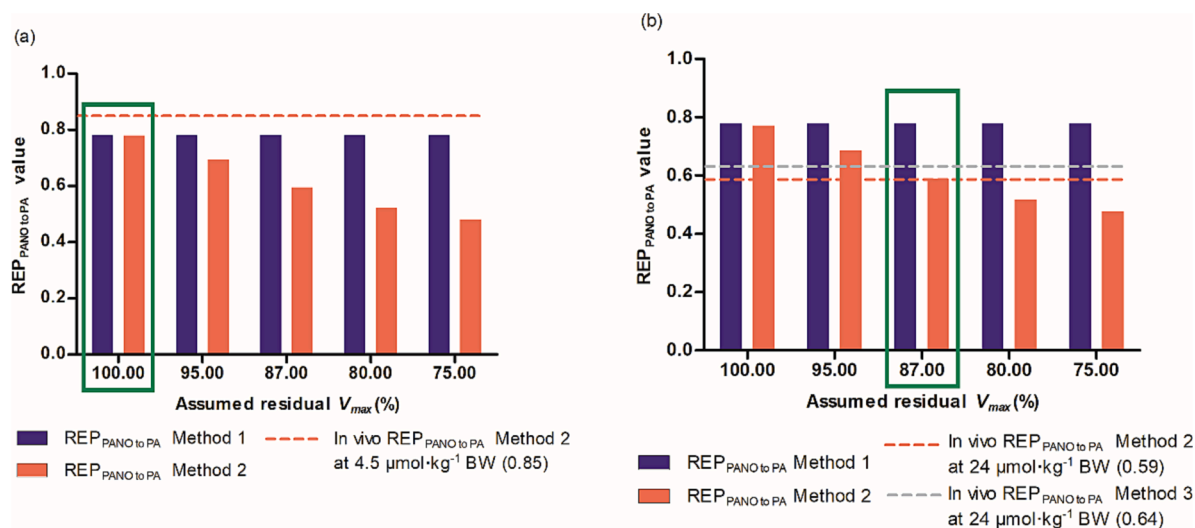**Fig. 5.** REP$_{PANO\ to\ PA}$ values when calculated based on PBK-modeling based predictions with increasing reduction in V_{max} for 7-GS-DHP formation when dosing RID because of GSH depletion. PBK model simulations were performed assuming a dose level of a) 4.5 and b) 24 μmol·kg^{-1} BW of RIDO and RID as used by Xia et al. (Xia et al., 2016) in their in vivo rat study, 15 % bioavailability, 0.40 as fraction bioactivated to pyrrole intermediates (f), and using either the AUC of RID (Method 1, Fig. 1, blue bars) or the amount of pyrrole-protein adducts (Method 2, Fig. 1, red bars). The reduction in V_{max} (reflected by the assumed % residual V_{max}) mimics the consequences of GSH depletion for the pyrrole scavenging by GSH upon dosing RID. The orange and grey horizontal lines represent the REP$_{PANO\ to\ PA}$ values derived from the in vivo study by Xia et al. (Xia et al., 2016) and Xia et al. (Xia et al., 2013), respectively (Table 1). (For interpretation of the references to colour in this figure legend, the reader is referred to the web version of this article.)
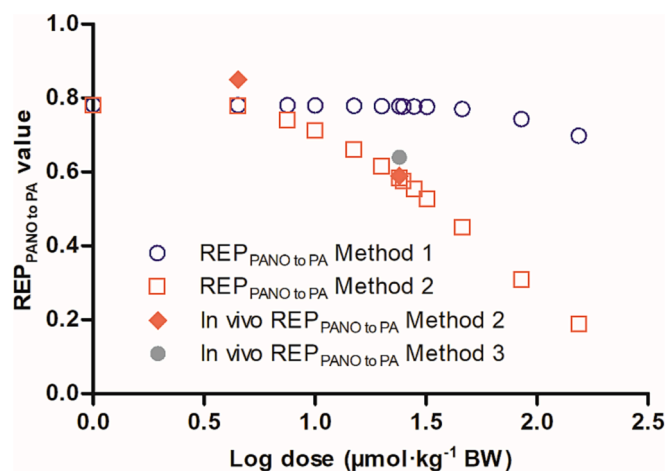

Fig. 6. PBK-simulated REP$_{PANO\ to\ PA}$ values of RIDO compared to RID using different endpoints across a range of dose levels using an f value of 0.40. In vivo REP$_{PANO\ to\ PA}$ values for Method 2 and Method 3 were calculated as shown in Table 1 and are presented for comparison.

onwards than that for Method 2.

To explain these changes in some more detail, Fig. 7a presents the dose-normalized changes in the clearance of RID upon dosing RID and in the reduction of RIDO with increasing dose levels as calculated by the PBK model of the present study. This reveals that with increasing dose of RID, at dose levels above 32 μmol·kg^{-1} BW, its clearance in the liver saturates resulting in relatively higher AUC values for RID. At the same time, with increasing equimolar dose of RIDO the reduction of RIDO to RID by the intestinal microbiota saturates, resulting in a relative lower AUC for RID at increasing dose levels. Together, these two phenomena can explain the reduced REP$_{PANO\ to\ PA}$ value with increasing dose levels as calculated by Method 1 based on AUC values.

To further investigate the more pronounced reduction in the REP$_{PANO\ to\ PA}$ value with the dose when calculated by Method 2, Fig. 7b shows the change in the dose-normalized amounts of 7-GS-DHP and pyrrole-protein adducts formed upon oral dosing an increasing amount

of RIDO and RID. Especially upon dosing RID, a relatively higher formation of the pyrrole-protein adducts at the cost of 7-GS-DHP adducts is observed at dose levels > 4.5 μmol·kg^{-1} BW, the dose level at which GSH is not depleted. This effect is not observed upon dosing RIDO, resulting in a dose dependent decrease in the REP$_{PANO\ to\ PA}$ value calculated by Method 2 already at dose levels > 4.5 μmol·kg^{-1} BW onwards. Internal GSH depletion does not influence the REP$_{PANO\ to\ PA}$ value calculated by Method 1, for which the REP$_{PANO\ to\ PA}$ value starts to show a reduction with the dose above 32 μmol·kg^{-1} BW due to saturation of RID clearance and RIDO reduction (Fig. 7a).

Correlation between f and % residual V_{max}

A final topic considered was that the PBK model simulations presented so far were based on several assumptions including: i) the dose levels of 4.5 and 24 μmol·kg^{-1} BW, which were in line with the in vivo dose levels for which REP values could be derived, ii) 15 % bioavailability, which was supported by earlier modeling data where kinetics of RID were best simulated with 15 % bioavailability (Widjaja et al., 2022), but also iii) a fraction bioactivated (f) of 0.40. Using this f value of 0.40, the % residual V_{max} was fitted to adequately predict the in vivo REP$_{PANO\ to\ PA}$ values by the PBK model simulations. To obtain insight in the influence of the fraction bioactivated, further simulations were performed.

These simulations were first done at a dose level of 24 μmol·kg^{-1} BW using the in vivo REP$_{PANO\ to\ PA}$ of 0.59 at this dose level for fitting of the % residual V_{max} to adequately predict this REP$_{PANO\ to\ PA}$ value at different values for f. Fig. 8a shows the results obtained and reveals that at 24 μmol·kg^{-1} BW, the REP$_{PANO\ to\ PA}$ value of 0.59 obtained by Method 2 can be equally well predicted when using different combinations of f and % residual V_{max}. It is clear from Fig. 8a that the combinations of f and % residual V_{max} that result in adequate predictions are linearly correlated with a negative slope, reflecting that at a higher f more of the initial dose is bioactivated, hence the GSH depletion resulting from pyrrole formation at a given dose will be higher, resulting in a lower % residual V_{max} for 7-GS-DHP formation.

Fig. 8b presents the results from similar analyses as the one presented in Fig. 8a but performed at different dose levels. The slope, Y-intercept and X-intercept values of these linear regression lines can be found in Table 9S of the Supplementary Material. Fig. 8 reveals that the change in
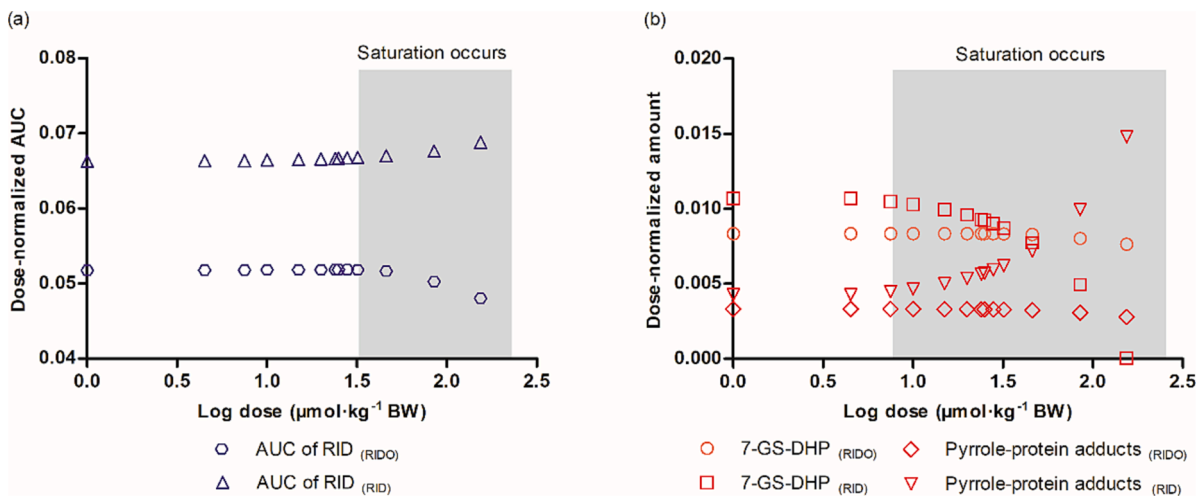
Fig. 7. Dose-normalized a) AUC of RID and b) amount of 7-GS-DHP and pyrrole-protein adducts from oral RIDO or equimolar dose of oral RID administration at an f value of 0.40. Grey box indicates the dose level where saturation of reactions occurs, causing the $REP_{PANO\ to\ PA}$ value to decrease with increasing dose. Note the different y-axis scale, particularly for (a) where the y-axis starts from 0.04 instead of 0.00.
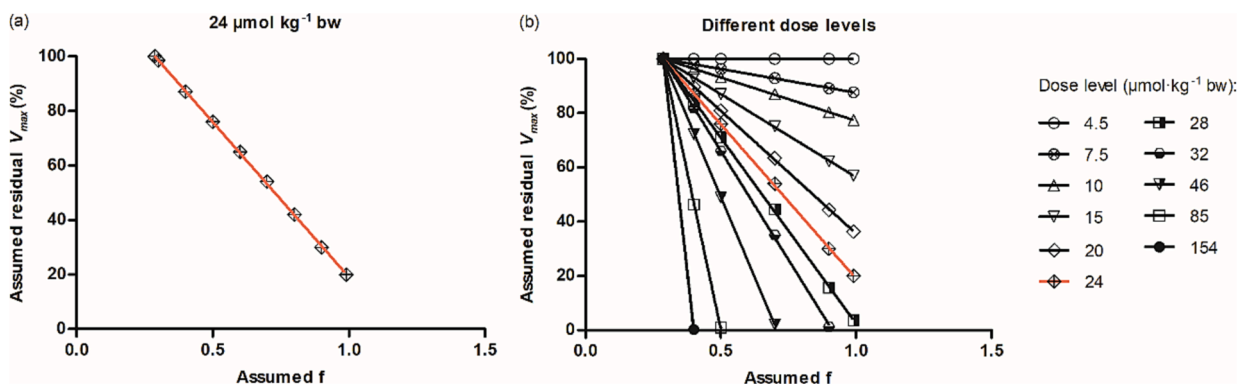

Fig. 8. Correlation between assumed f and assumed % residual V_{max} at a) 24 µmol·kg^{-1} BW (red line) and b) different dose levels of RIDO and an equimolar dose of RID with 15 % bioavailability that result in the PBK-simulated based $REP_{PANO\ to\ PA}$ value by Method 2 of 0.59. Note that the f value is capped at 1.0, and 100 % residual V_{max} was assumed for 4.5 µmol·kg^{-1} BW and different % residual V_{max} at 24 µmol·kg^{-1} BW were obtained to predict the $REP_{PANO\ to\ PA}$ value depending on the f value used, all in all resulting in a PBK-simulated based $REP_{PANO\ to\ PA}$ value by Method 2 of 0.59 at 24 µmol·kg^{-1} BW. (For interpretation of the references to colour in this figure legend, the reader is referred to the web version of this article.)
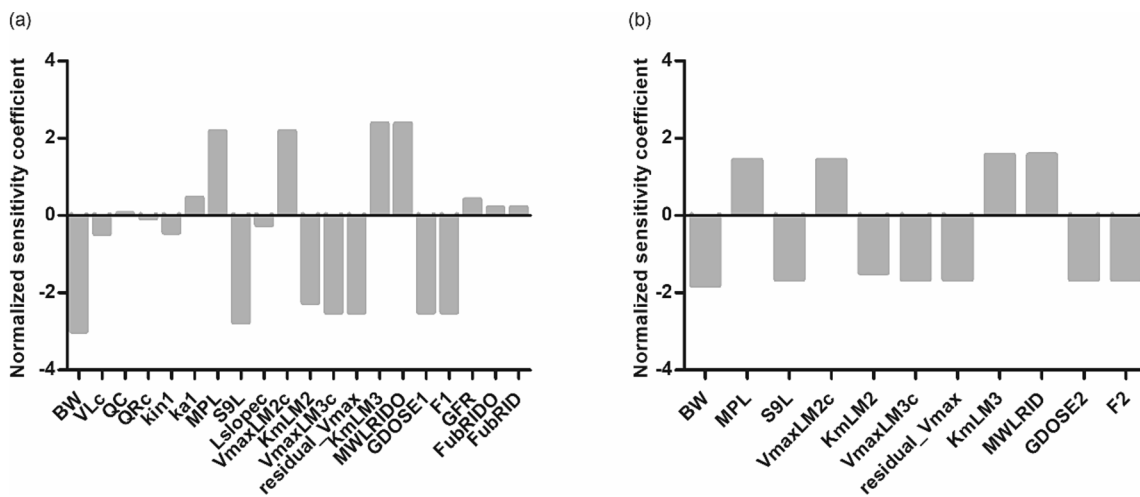

Fig. 9. Normalized SCs for the parameters of the rat PBK model for a) RIDO and b) RID dosage on predicted amount$_{pyrrole-protein\ adducts}$ (µmol) at equimolar doses of 24 µmol·kg^{-1} BW. The assumed % residual V_{max} at this dose level was 100 % and 87 % for RIDO and RID, respectively. The complete list of abbreviations can be found in Table 3S of the Supplementary Material.

f value is not influential for the $REP_{PANO\ to\ PA}$ value obtained by Method 2 because changing the *f* values is accompanied by changing the % residual V_{max}. It is also important to note that at low dose level different *f* values all result in an adequate prediction of the $REP_{PANO\ to\ PA}$ value assuming 100 % residual V_{max}, hence the *f* value no longer influences the $REP_{PANO\ to\ PA}$ value.

Sensitivity analysis

To evaluate which parameters are influential to the amount$_{pyrrole-protein\ adducts}$, normalized SCs were calculated for both the RIDO and RID model at a dose of 24 μmol·kg^{-1} BW resulting in the data shown in Fig. 9. Similar results were obtained for both models, where the parameters of influence on the model prediction for the amount$_{pyrrole-protein\ adducts}$ were those involved in RID clearance (MPL, VmaxLM2c, KmLM2) and 7-GS-DHP formation (S9L, VmaxLM3c, residual_Vmax, and KmLM3c). In the RIDO model, parameters other than those mentioned are also shown, but they appeared to have a substantially lower influence with SC values < |1|. It is worth noting that the parameters that are negatively related to 7-GS-DHP were positively related to the amount of pyrrole-protein adducts and *vice versa*.

Three other PA-N-oxides and PAs

Upon evaluation and validation of the PBK modeling approach to quantify the $REP_{PANO\ to\ PA}$ value for RIDO and the previous validation of the method for predicting the $REP_{PANO\ to\ PA}$ value for SENO (Widjaja et al., 2023; Widjaja et al., 2023), additional studies were performed to predict the $REP_{PANO\ to\ PA}$ values for three other macrocyclic diester PANOs including SNPO, RTRO and SVRO.

Kinetic constants from in vitro incubations

Fig. 10 presents the in vitro kinetic data of PA-N-oxide reduction of SNPO, RTRO and SVRO to their parent PAs by gut microbiota and by liver S9, as well as the clearance of the corresponding PAs and 7-GS-DHP formation from these PAs. PA-N-oxide reduction by gut microbiota and PA clearance by liver S9 follow Michaelis-Menten kinetics, while PA-N-oxide reduction by liver S9 follows first-order kinetics. The kinetic constants obtained from these data are presented in Tables 4 and 5. For PA-N-oxide reduction by gut microbiota, the scaled $k_{cat\ in\ vivo}$ values for SNPO, RTRO and SVRO were 14.5-, 3.9- and 5.5-fold lower than that obtained for RIDO, respectively. For PA-N-oxide reduction by rat liver S9, the scaled $k_{cat\ in\ vivo}$ value for SNPO, RTRO and SVRO were 2.5-, 1.8- and 1.8-fold higher than for RIDO. Concerning the PA clearance, the scaled $k_{cat\ in\ vivo}$ value for SNP was 1.05-fold lower than for RID, whereas the scaled $k_{cat\ in\ vivo}$ values for RTR and SVR were 1.12- and 3.02-fold higher than that obtained for RID, respectively. For 7-GS-DHP formation from the parent PAs, the scaled $k_{cat\ in\ vivo}$ values for SNP, RTR and SVR were 2.61-, 2.25- and 2.43-fold lower than that for RID, respectively. Concentrations of SNP, RTR and SVR in the liver as predicted by the PBK model at relatively high dose levels of 24 μmol·kg^{-1} BW amount
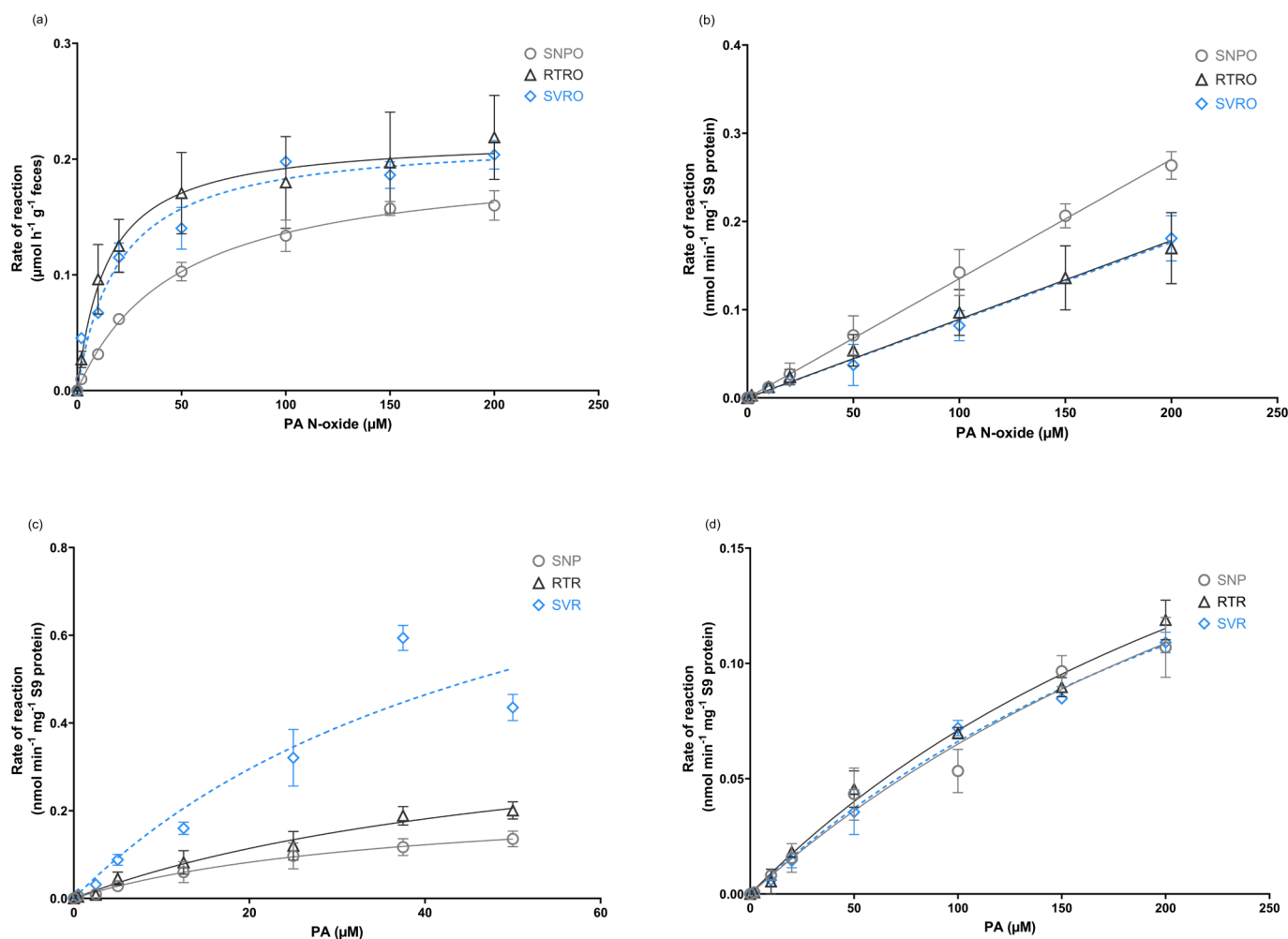

Fig. 10. PA-N-oxide concentration dependent rate of conversion of PA-N-oxides to PAs in a) anaerobic rat fecal incubations and b) aerobic rat liver S9 incubations, and PA concentration dependent rate of c) PA clearance and d) 7-GS-DHP formation in aerobic rat liver S9 incubations. Data are presented as mean ± SD of three independent experiments (n = 3).

Table 4

Kinetic constants for the reduction of PA-N-oxides by rat gut microbiota.

Compound	$V_{max, in vitro}$ ($\mu mol \cdot h^{-1} \cdot g^{-1}$ feces)	$V_{max, in vivo}$ ($\mu mol \cdot h^{-1}$)[a]	K_m (μM)	$k_{cat, in vitro}$ ($L \cdot h^{-1} \cdot g^{-1}$ feces)[b]	$k_{cat, in vivo}$ ($L \cdot h^{-1}$)[c]
SNPO	0.2013	0.825	47.94	0.0042	0.0172
RTRO	0.2200	0.902	14.34	0.0153	0.0629
SVRO	0.2191	0.898	19.77	0.0111	0.0454
RIDO[d]	0.1600	0.656	2.63	0.0608	0.2490

a) $V_{max, in vivo} = (V_{max, in vitro}) \times fbw \times BW \times 1000$. Rat fraction of feces to BW (fbw) is 0.0164 g feces g^{-1}·BW and rat BW is 0.25 kg; b) $k_{cat, in vitro} = (V_{max, in vitro})/K_m$; c) $k_{cat, in vivo} = (V_{max, in vivo})/K_m$; d) Data from previous study (Widjaja et al., 2022).

to 0.23 µM, 0.34 µM and 0.09 µM (from oral PA-N-oxide dosing) and 1.24 µM, 0.78 µM and 0.21 µM (from an equimolar oral dose of PA); all of these values are significantly lower than the respective K_m values for 7-GS-DHP formation (Table 5). This is similar to what has been observed for RID in section 3.1.1, corroborating that limitations in 7-GS-DHP formation are unlikely to result from saturation of the enzyme kinetics, and might rather be due to GSH depletion at high dose PA.

To evaluate the PBK models for the three additional macrocyclic diester PA-N-oxides and their PAs, only limited in vivo data are available, consisting of in vivo rat data on blood concentrations upon an oral

dose of SNP (Long et al., 2021) and RTR (Ma et al., 2021). Fig. 11 presents the comparison of PBK model based predictions and available in vivo data for SNP and RTR blood concentrations, also presenting the PBK model predicted PA blood concentrations upon dosing the corresponding PA-N-oxide. For SNP, the best fit for the PBK model simulations was achieved assuming 10 % bioavailability upon the reported SNP oral dose of 20 mg·kg^{-1} BW. The predicted $C_{max SNP}$ was 1.2-fold lower than the reported in vivo $C_{max SNP}$. The predicted time to reach maximum blood concentration (T_{max}) was 1.7-fold lower than the reported in vivo $T_{max SNP}$ (Fig. 11a and Table 5S Supplementary Materials). For RTR, the prediction was best fitted to the in vivo data when assuming 24 % bioavailability at a reported RTR oral dose of 40 mg·kg^{-1} BW. The predicted $C_{max RTR}$ and $T_{max RTR}$ were 1.03- and 1.6-fold higher than the reported animal data (Fig. 11b and Table 7S Supplementary Materials). For SVR, no in vivo data for PBK model evaluation were available, hence validation of this model was based on validation of the same model for SEN (Widjaja et al., 2023; Widjaja et al., 2023), RID (Widjaja et al., 2022) and SNP and RTR in the present study. Fig. 11c presents the PBK model predicted SVR blood concentrations upon dosing 8.4 mg·kg^{-1} BW of SVR or an equimolar dose of SVRO.

Using the PBK models thus obtained and validated, the REP$_{PANO\ to\ PA}$ values of RTRO, SNPO and SVRO by both Method 1 and 2 were calculated and are shown in Fig. 12. At high dose level such as 154 µmol·kg^{-1} BW, the REP$_{PANO\ to\ PA}$ for RTRO, SNPO and SVRO are 0.81, 0.69, and

Table 5

Kinetic constants for the reduction of PA-N-oxides, clearance of parent PAs and formation of 7-GS-DHP in incubations with rat liver S9 and scaled to the in vivo situation.

Compound	$V_{max, in vitro}$ (nmol·min^{-1}·mg^{-1} S9 protein)	$V_{max, in vivo}$ ($\mu mol \cdot h^{-1}$)[a]	K_m (μM)	$k_{cat, in vitro}$ (mL·min^{-1}·mg^{-1} S9 protein)[b]	$k_{cat, in vivo}$ (L·h^{-1})[c]
Reduction of PA-N-oxide to parent PAs by rat liver S9					
SNPO	n.a.	n.a.	n.a.	0.0013	0.0948
RTRO	n.a.	n.a.	n.a.	0.0009	0.0656
SVRO	n.a.	n.a.	n.a.	0.0009	0.0656
RIDO[d]	n.a.	n.a.	n.a.	0.0005	0.0370
Clearance of PAs by rat liver S9					
SNP	0.24	17.50	37.52	0.0064	0.4664
RTR	0.44	32.09	57.64	0.0076	0.5567
SVR	1.10	80.22	53.68	0.0205	1.4944
RID[d]	2.093 nmol·min^{-1}·mg^{-1} microsome protein[d]	37.36	75.69	0.0277 mL·min^{-1}·mg^{-1} microsome protein[d]	0.4936
Formation of 7-GS-DHP by rat liver S9					
SNP	0.33	24.10	412.0	0.0008	0.0584
RTR	0.31	22.61	333.0	0.0009	0.0679
SVR	0.30	21.88	347.7	0.0009	0.0629
RID	0.17	12.40	81.20	0.0021	0.1526

a) $V_{max, in vivo} = [(V_{max, in vitro}) / 1000] \times 60 \times [S9\ in\ liver] \times [liver\ weight] \times BW$. Rat S9 is 143 mg S9 protein·g^{-1} liver, the weight of rat liver is 34 g·kg^{-1} BW and rat body weight is 0.25 kg; b) $k_{cat, in vitro} = (V_{max, in vitro}) / K_m$; c) $k_{cat, in vivo} = (V_{max, in vivo}) / K_m$; d) Data of RIDO reduction by rat liver S9 taken from Widjaja et al. (Widjaja et al., 2022) while data of RID clearance by rat liver microsome taken from Chen et al. (Chen et al., 2018) with *[Microsome in liver]* of 35 mg microsome protein·g^{-1} liver.
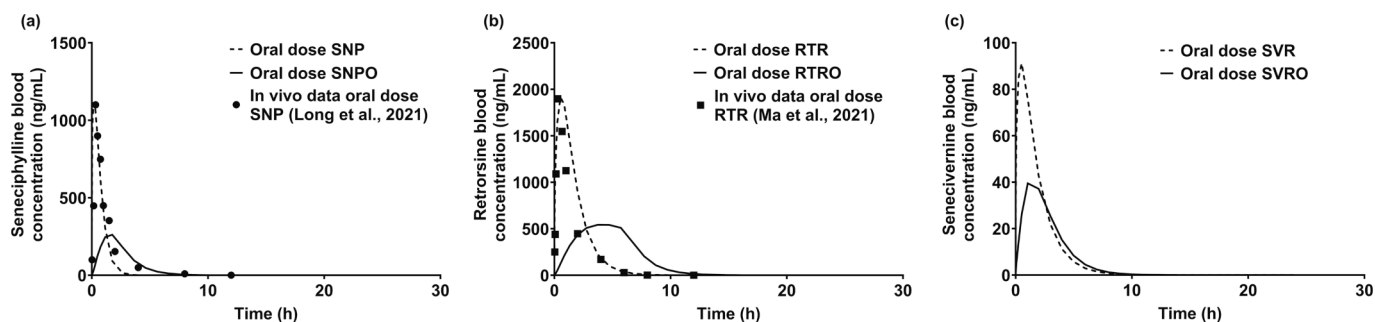

Fig. 11. Comparison of literature available rat in vivo data and PBK model based predictions for: (a) SNP blood concentrations reported by Ma et al., 2021 (circles) and predicted assuming 10 % bioavailability at an oral dose of 20 mg·kg^{-1} BW for SNP (dashed line) or an equimolar dose of SNPO (continuous line); (b) RTR blood concentration reported by Long et al., 2021 (squares) and predicted assuming 24 % bioavailability at an oral dose of 40 mg·kg^{-1} BW for RTR (dashed line) or an equimolar dose of RTRO (continuous line); and (c) predicted SVR blood concentrations assuming 15 % bioavailability at an oral dose of 8.4 mg·kg^{-1} BW for SVR (dashed line) or an equimolar dose of SVRO (continuous line).
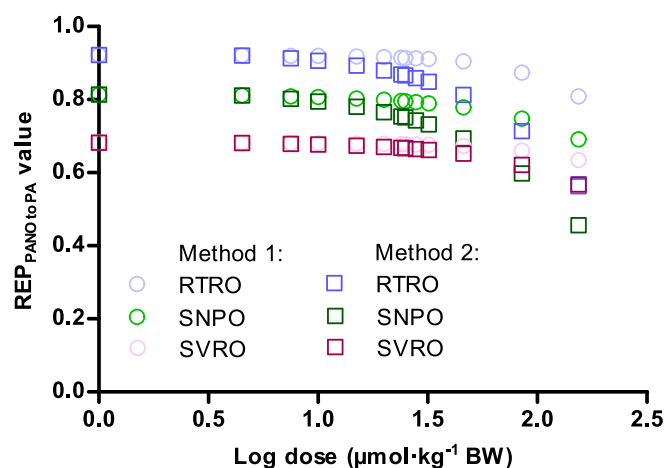
Fig. 12. PBK-simulated REP$_{PANO\ to\ PA}$ values of the three other PA-N-oxides with f of 0.4 and with % residual V_{max} of 87 % at 24 μmol·kg^{-1} BW.

0.63 (Method 1) and 0.56, 0.46, and 0.57 (Method 2). At 24 μmol·kg^{-1} BW, the REP$_{PANO\ to\ PA}$ for RTRO, SNPO and SVRO increase to 0.91, 0.80 and 0.68 (Method 1) and 0.87, 0.75 and 0.67 (Method 2). At low dose level, the REP$_{PANO\ to\ PA}$ values of RTRO, SNPO and SVRO are equal for both Method 1 and 2, amounting to 0.92, 0.81 and 0.68, respectively.

Discussion

Data from previous studies on RIDO and RID in rats (Yang et al., 2019; Xia et al., 2016; Xia et al., 2013; Williams et al., 2002) revealed that the REP$_{PANO\ to\ PA}$ value of RIDO relative to its parent PA RID varied with the endpoint used (Table 1). The REP$_{PANO\ to\ PA}$ value based on comparison of the amount of pyrrole-protein adducts at 4.5 μmol·kg^{-1} BW yielded a higher value of 0.85 than the REP$_{PANO\ to\ PA}$ value of 0.59 at the higher dose of 24 μmol·kg^{-1} BW (Xia et al., 2016). When calculated based on comparison of the AUC of formed RID (Method 1), the REP$_{PANO\ to\ PA}$ value derived from available in vivo data of 0.32 (Table 1) deviated from the predicted value of 0.78, but this may be related to the fact that the available in vivo data came from two different studies, with different dose levels and different strains of rats (Yang et al., 2019; Williams et al., 2002). When calculated based on comparison of pyrrole-protein adducts at 4.5 μmol·kg^{-1} BW, the in vivo REP$_{PANO\ to\ PA}$ value of 0.85 was close to the predicted REP$_{PANO\ to\ PA}$ value of 0.78. Moreover, when calculated based on comparison of the amount of pyrrole-DNA adducts at 24 μmol·kg^{-1} BW, the REP$_{PANO\ to\ PA}$ value of 0.64 was comparable to the one calculated from the amount of pyrrole-protein adducts of 0.59 at the same dose. Thus, the PBK-simulated REP$_{PANO\ to\ PA}$ values for RIDO matched the available in vivo data for Method 2 and confirmed the dose dependency of this REP value, decreasing with increasing dose. In further studies of the present paper, PBK modeling was used to investigate the effect of dose and endpoint used on the REP$_{PANO\ to\ PA}$ value for RIDO also testing the hypothesis that the lower REP$_{PANO\ to\ PA}$ value obtained by Method 2 could be ascribed to limitation of the 7-GS-DHP formation capacity upon high internal PA concentrations, a situation previously shown to influence amount of pyrrole-protein adducts from SEN (Widjaja et al., 2023).

Results obtained indicated that up to 400 μM RID, the 7-GS-DHP formation from RID showed Michaelis-Menten kinetics with an in vitro k$_{cat}$ value amounting to 0.0021 mL·min^{-1}·mg S9 protein scaled to an in vivo k$_{cat}$ value amounting to 0.1527 L·h^{-1}. Ning et al. (Ning et al., 2019; Ning et al., 2019) also measured 7-GS-DHP formation from RID in incubations with Caucasian human liver microsomes, and reported an in vivo k$_{cat}$ value of 0.2253 L·h^{-1}, comparable (1.5-fold higher) to the one obtained in the present study from rat liver S9. Inter-species differences in kinetics and liver toxicity of the pyrrolizidine alkaloids are known to

exist and have previously been studied for lasiocarpine and RID (Ning et al., 2019). Based on the benchmark dose lower and upper confidence limits for 5 % effect (BMDL5 and BMDU5), the inter-species differences were 2.0-fold for lasiocarpine and 8.2-fold for RID with humans being more sensitive than rats (Ning et al., 2019). Recently, we measured 7-GS-DHP formation in rat liver S9 from SEN (Widjaja et al., 2022), a retronecine type PA similar to RID that also belongs to the macrocyclic diester PA group. The kinetic values for RID and SEN were highly comparable, with the rate of 7-GS-DHP from SEN being 1.1-fold higher than that obtained in the present study for RID. This difference was somewhat smaller than that reported by He et al. (He et al., 2021) who found upon incubation of rat primary hepatocytes with 50 μM RID or SEN for 24 h, up to 3.2-fold higher 7-GS-DHP and 2.5-fold higher total adduct formation from RID compared to SEN. The difference in incubation time, 1 h in our work compared to 24 h, as well as the usage of liver S9 compared to liver hepatocytes, or a potential difference in the CYPs present in the respective liver preparations may explain the difference although this remains to be investigated.

REP$_{PANO\ to\ PA}$ values based on pyrrole-protein adducts were also calculated for SEN (Widjaja et al., 2023) with an f (fraction bioactivated) of 0.2 and a % residual V_{max} of 63 % to reach the in vivo REP$_{PANO\ to\ PA}$ value of 0.61 at 55 μmol·kg^{-1} BW SENO and an equimolar dose of SEN (Yang et al., 2017). In previous work with SEN, the correlation between f and the % residual V_{max} (i.e. or % residual k$_{cat}$ because 7-GS-DHP formation from tested SEN concentration was a first order reaction) was not studied, and there was only one dose level to validate the model prediction (i.e. 55 μmol·kg^{-1} BW). In the current simulations for RID, f and % residual V_{max} were shown to be negatively correlated, and two dose levels were used; 4.5 μmol·kg^{-1} BW with predicted REP$_{PANO\ to\ PA}$ values matching the in vivo value at 100 % residual V_{max} (no GSH depletion) and 24 μmol·kg^{-1} BW with the REP$_{PANO\ to\ PA}$ value of 0.59 being adequately predicted at 87 % residual V_{max} value due to GSH depletion. In the present simulations the reduction in GSH levels and V_{max} were assumed to start from 4.5 μmol·kg^{-1} BW onwards although formally the GSH depletion could also start at higher dose levels but that will not affect the outcomes at 24 μmol·kg^{-1} BW where a % residual V_{max} of 87 % was shown to best fit the experimental data for the REP$_{PANO\ to\ PA}$ value of RIDO to RID.

The results of the present study also revealed that not only the REP$_{PANO\ to\ PA}$ value calculated by Method 1 but also the REP$_{PANO\ to\ PA}$ value calculated by Method 2 decreases with increasing dose levels. For Method 1 this was shown to be due to saturation of RID clearance and RIDO reduction, while for Method 2 it appeared to be due to reduction of the GSH scavenging of the pyrrole intermediate with higher dose, but also with higher % bioavailability or higher fraction bioactivated, all resulting in increased GSH depletion due to the higher amounts of reactive pyrrole intermediates. This is in agreement with previous literature showing in vitro concentration-dependent GSH depletion upon PA exposure (Griffin and Segall, 1987; Neuman et al., 2007; Chen et al., 2009; Wang et al., 2000; Ji et al., 2008; Yang et al., 2016; Yang et al., 2017; Xiong et al., 2020).

In spite of this decrease in REP$_{PANO\ to\ PA}$ values with increasing dose, the PBK modeling also revealed that at lower dose levels, such as dose levels of 5–10 ng·kg^{-1} BW that are more in the range of human dietary intake of PAs (EFSA et al., 2017), the REP$_{PANO\ to\ PA}$ value for RIDO tends to converge to a value of 0.78. At these low dose levels, also the fraction bioactivated no longer influences the REP$_{PANO\ to\ PA}$ value since it appeared from the results of the present study that at low dose levels GSH depletion will not occur, not even at high values for f. It is of interest to note that this REP$_{PANO\ to\ PA}$ value that is relevant at low dose levels and thus most relevant in the range of human dietary intake of PAs will be difficult to determine in an animal experiment given the detection limits for quantification of the pyrrole-protein adducts. It is also of interest to note that the current REP$_{PANO\ to\ PA}$ values were based on rat data and a rat PBK model, but that PBK modeling also provides a way to determine the REP value for human since the method applied uses only

in silico and in vitro data to support the PBK model predictions (Widjaja et al., 2023).

Furthermore, given that the approach now has been proven adequate for two PAs for which in vivo data to evaluate the $REP_{PANO\ to\ PA}$ predictions are available, and the fact that in both cases it has been shown that at low dose levels the bioavailability or fraction bioactivated no longer influence the $REP_{PANO\ to\ PA}$ value outcome, it can be concluded that this approach can be used to predict low dose $REP_{PANO\ to\ PA}$ values for also other PA-N-oxides for which in vivo data to evaluate the predicted $REP_{PANO\ to\ PA}$ values are absent. To this end, first PBK models were defined for these PA-N-oxides and their PAs using in vitro and in silico methods to define the respective parameters. Literature available data on blood PA concentrations in rats for SNP and RTR enabled validation of these PBK models also corroborating the validity of the PBK model as such for other PAs than RID and SEN. The PBK model was subsequently used to simulate the $REP_{PANO\ to\ PA}$ values for the three additional macrocyclic PAs. The results obtained reveal that the $REP_{PANO\ to\ PA}$ of SNPO, RTRO and SVRO calculated by Method 1 and Method 2 at low dose level amounted to 0.81, 0.92 and 0.68, respectively, while the $REP_{PANO\ to\ PA}$ for RIDO amounted to 0.78. Overall, the $REP_{PANO\ to\ PA}$ values of the tested PA-N-oxides and PAs follow the order: RTRO > SNPO ≈ RIDO > SVRO.

The current study corroborates that the dose and endpoint used influence the $REP_{PANO\ to\ PA}$ value, but also elucidates that and why the fraction bioactivated is not of influence. This is important because this parameter is generally difficult to quantify in either in vivo or in vitro studies. Given these results, the current approach provides a way forward to define $REP_{PANO\ to\ PA}$ values of PA-N-oxides at low dose levels realistic for human intake. Since the $REP_{PANO\ to\ PA}$ values converge to a single value that is independent of endpoint at low dose levels, $REP_{PANO\ to\ PA}$ values can be calculated based on the AUC of the PA (Endpoint 1), which will require less data and only in vitro studies to define the kinetic parameters for PA-N-oxides reduction by intestinal microbiota and liver samples, and hepatic PA clearance.

The $REP_{PANO\ to\ PA}$ values for the PA-N-oxides relative to their parent PAs obtained by the new approach methodology can subsequently be used to establish REP values for the PA-N-oxides relative to the reference PA RID ($REP_{PANO\ to\ RID}$). To this end, the $REP_{PANO\ to\ PA}$ should be multiplied by the REP value for the respective PA relative to RID ($REP_{PA\ to\ RID}$). Given that RID is the reference PA for RIDO, the $REP_{PANO\ to\ PA}$ is per definition equal to the $REP_{PANO\ to\ RID}$ because the $REP_{PA\ to\ RID}$ for RID equals 1.00. Meanwhile, for other PAs, the $REP_{PA\ to\ RID}$ can be obtained using in vitro methods since for these REP values for parent PAs there is no role of intestinal microbial metabolism. For use in risk assessment it appears essential to determine the low dose $REP_{PANO\ to\ RID}$ values for the different PA-N-oxides, as done in the present study, because ultimately $REP_{PANO\ to\ RID}$ values should be valid for real life risk assessment of exposure to low dose mixtures of PAs and PA-N-oxides.

In summary, PBK modeling can be used to investigate the mechanism behind the dose and particularly endpoint dependent $REP_{PANO\ to\ PA}$ value. At low dose levels, the $REP_{PANO\ to\ PA}$ value appears to be independent of the endpoint used. In contrast, at high dose levels as used in animal studies that would enable experimental determination of $REP_{PANO\ to\ PA}$ values, the $REP_{PANO\ to\ PA}$ values based on formed PAs are higher than the ones based on pyrrole-DNA or pyrrole-protein adducts as seen for RIDO. The limited capacity of GSH in scavenging reactive pyrrole intermediates is due to GSH depletion upon dosing the parent PAs, which causes the $REP_{PANO\ to\ PA}$ value determined by pyrrole-protein adducts to drop faster than the REP value based on formed PAs. Finally, our work demonstrates the strength of using a new approach methodology based on PBK modeling to replace, reduce and refine (3R) the use of animal testing in predicting the $REP_{PANO\ to\ PA}$ values based on different endpoints also at low dose levels that are experimentally less accessible in animal studies.

CRediT authorship contribution statement

Yasser Alhejji: Conceptualization, Formal analysis, Investigation, Methodology, Data curation, Software, Validation, Visualization, Writing – original draft. **Frances Widjaja:** Conceptualization, Formal analysis, Investigation, Methodology, Data curation, Software, Validation, Visualization, Writing – original draft. **Shenghan Tian:** Formal analysis, Investigation, Methodology, Data curation, Software, Validation, Visualization, Writing – review & editing. **Thomas Hoekstra:** Formal analysis, Investigation, Methodology, Data curation, Validation, Visualization, Writing – review & editing. **Sebastiaan Wesseling:** Formal analysis, Investigation, Methodology, Resources, Validation, Writing – review & editing. **Ivonne M.C.M. Rietjens:** Conceptualization, Formal analysis, Funding acquisition, Investigation, Project administration, Software, Supervision, Validation, Writing – review & editing.

Declaration of competing interest

The authors declare that they have no known competing financial interests or personal relationships that could have appeared to influence the work reported in this paper.

Data availability

I have shared the model code as supplementary information in the Attach file stage.

Appendix A. Supplementary data

Supplementary data to this article can be found online at https://doi.org/10.1016/j.crtox.2024.100160.

References

Allemang, A., Mahony, C., Lester, C., Pfuhler, S., 2018. Relative potency of fifteen pyrrolizidine alkaloids to induce DNA damage as measured by micronucleus induction in HepaRG human liver cells. Food Chem. Toxicol. 121, 72–81.

Chen, Y., Ji, L., Wang, H., Wang, Z., 2009. Intracellular glutathione plays important roles in pyrrolizidine alkaloids-induced growth inhibition on hepatocytes. Environ. Toxicol. Pharmacol. 28 (3), 357–362.

Chen, L., Ning, J., Louisse, J., Wesseling, S., Rietjens, I.M.C.M., 2018. Use of physiologically based kinetic modelling-facilitated reverse dosimetry to convert in vitro cytotoxicity data to predicted in vivo liver toxicity of lasiocarpine and riddelliine in rat. Food Chem. Toxicol. 116, 216–226.

Chen, Y., Xiong, F., Wang, W., Jiang, K., Ye, X., Deng, G., et al., 2020. The long persistence of pyrrolizidine alkaloid-derived pyrrole-protein adducts in vivo: kinetic study following multiple exposures of a pyrrolizidine alkaloid containing extract of Gynura japonica. Toxicol. Lett. 323, 41–47.

Chou MW, Yan J, Nichols J, Xia Q, Beland FA, Chan P-C, et al. Correlation of DNA adduct formation and riddelliine-induced liver tumorigenesis in F344 rats and B6C3F1 mice [Cancer Lett. 193 (2003) 119–125]. Cancer Lett. 2004;207(1):119-25.

Chou, M.W., Wang, Y.-P., Yan, J., Yang, Y.-C., Beger, R.D., Williams, L.D., et al., 2003. Riddelliine N-oxide is a phytochemical and mammalian metabolite with genotoxic activity that is comparable to the parent pyrrolizidine alkaloid riddelliine. Toxicol. Lett. 145 (3), 239–247.

Dusemund, B., Nowak, N., Sommerfeld, C., Lindtner, O., Schäfer, B., Lampen, A., 2018. Risk assessment of pyrrolizidine alkaloids in food of plant and animal origin. Food Chem. Toxicol. 115, 63–72.

EFSA, Knutsen, H.K., Alexander, J., Barregård, L., Bignami, M., Brüschweiler, B., et al., 2017. Risks for human health related to the presence of pyrrolizidine alkaloids in honey, tea, herbal infusions and food supplements. EFSA J. 15 (7), e04908.

Griffin, D.S., Segall, H., 1987. Role of cellular calcium homeostasis in toxic liver injury induced by the pyrrolizidine alkaloid senecionine and the alkenal trans-4-OH-2-hexenal. J. Biochem. Toxicol. 2 (3), 155–167.

He, X., Xia, Q., Woodling, K., Lin, G., Fu, P.P., 2017. Pyrrolizidine alkaloid-derived DNA adducts are common toxicological biomarkers of pyrrolizidine alkaloid N-oxides. J. Food Drug Anal. 25 (4), 984–991.

He, X., Xia, Q., Shi, Q., Fu, P.P., 2021. Metabolism of carcinogenic pyrrolizidine alkaloids and pyrrolizidine alkaloid N-oxides by rat primary hepatocytes generate the same characteristic DHP-DNA adducts. J. Environ. Sci. Health C. 39 (4), 357–372.

Hoskins, L.C., Zamcheck, N., 1968. Bacterial degradation of gastrointestinal mucins: I. comparison of mucus constituents in the stools of germ-free and conventional rats. Gastroenterology 54 (2), 210–217.

Ji, L., Chen, Y., Wang, Z., 2008. Intracellular glutathione plays important roles in pyrrolizidine alkaloid clivorine-induced toxicity on L-02 hepatocytes. Toxicol. Mech. Methods 18 (8), 661–664.

Long, F., Ji, J., Wang, X., Wang, L., Chen, T., 2021. LC-MS/MS method for determination of seneciphylline and its metabolite, seneciphylline N-oxide in rat plasma and its application to a rat pharmacokinetic study. Biomed. Chromatogr 35 (9), e5145.

Louisse, J., Rijkers, D., Stoopen, G., Holleboom, W.J., Delagrange, M., Molthof, E., et al., 2019. Determination of genotoxic potencies of pyrrolizidine alkaloids in HepaRG cells using the γH2AX assay. Food Chem. Toxicol. 131, 110532.

Ma, J., Xia, Q., Fu, P.P., Lin, G., 2018. Pyrrole-protein adducts–a biomarker of pyrrolizidine alkaloid-induced hepatotoxicity. J. Food Drug Anal. 26 (3), 965–972.

Ma, J., Li, M., Li, N., Chan, W.Y., Lin, G., 2021. Pyrrolizidine alkaloid-induced hepatotoxicity associated with the formation of reactive metabolite-derived pyrrole-protein adducts. Toxins (basel). 13 (10), 723.

Ma, J., Zhang, C., He, Y., Chen, X., Lin, G., 2021. Fasting augments pyrrolizidine alkaloid-induced hepatotoxicity. Arch. Toxicol. 1–13.

Mattocks, A.R., 1971. Hepatotoxic effects due to pyrrolizidine alkaloid N-oxides. Xenobiotica 1 (4), 563–565.

Mendez-Catala, D.M., Wang, Q., Rietjens, I.M.C.M., 2021. PBK model-based prediction of intestinal microbial and host metabolism of zearalenone and consequences for its estrogenicity. Mol. Nutr. Food Res. 65 (23), 2100443.

Merz, K.-H., Schrenk, D., 2016. Interim relative potency factors for the toxicological risk assessment of pyrrolizidine alkaloids in food and herbal medicines. Toxicol. Lett. 263, 44–57.

Neuman, M.G., Jia, A.Y., Steenkamp, V., 2007. Senecio latifolius induces in vitro hepatocytotoxicity in a human cell line. Can. J. Physiol. Pharmacol. 85 (11), 1063–1075.

Ning, J., Chen, L., Strikwold, M., Louisse, J., Wesseling, S., Rietjens, I.M.C.M., 2019. Use of an in vitro–in silico testing strategy to predict inter-species and inter-ethnic human differences in liver toxicity of the pyrrolizidine alkaloids lasiocarpine and riddelliine. Arch. Toxicol. 93 (3), 801–818.

Ning, J., Rietjens, I.M.C.M., Strikwold, M., 2019. Integrating physiologically based kinetic (PBK) and Monte Carlo modelling to predict inter-individual and inter-ethnic variation in bioactivation and liver toxicity of lasiocarpine. Arch. Toxicol. 93 (10), 2943–2960.

Punt, A., Freidig, A.P., Delatour, T., Scholz, G., Boersma, M.G., Schilter, B., et al., 2008. A physiologically based biokinetic (PBBK) model for estragole bioactivation and detoxification in rat. Toxicol. Appl. Pharmacol. 231 (2), 248–259.

Ruan, J., Gao, H., Li, N., Xue, J., Chen, J., Ke, C., et al., 2015. Blood pyrrole-protein adducts—a biomarker of pyrrolizidine alkaloid-induced liver injury in humans. J. Environ. Sci. Health C 33 (4), 404–421.

Smith, L., Culvenor, C., 1981. Plant sources of hepatotoxic pyrrolizidine alkaloids. J. Nat. Prod. 44 (2), 129–152.

Stegelmeier, B.L., Edgar, J.A., Colegate, S.M., Gardner, D.R., Schoch, T.K., Coulombe, R. A., et al., 1999. Pyrrolizidine alkaloid plants, metabolism and toxicity. J. Nat. Toxins 8 (1), 95–116.

Tamta, H., Pawar, R.S., Wamer, W.G., Grundel, E., Krynitsky, A.J., Rader, J.I., 2012. Comparison of metabolism-mediated effects of pyrrolizidine alkaloids in a HepG2/C3A cell-S9 co-incubation system and quantification of their glutathione conjugates. Xenobiotica 42 (10), 1038–1048.

Tang, J., Wang, Z., Akao, T., Hattori, M., 2013. Human intestinal bacteria mediate reduction of the N-oxides of isoline and monocrotaline to the corresponding parent alkaloids. Asian J. Chem. 25 (4), 2027–2030.

Wang, X., Kanel, G.C., DeLeve, L.D., 2000. Support of sinusoidal endothelial cell glutathione prevents hepatic veno-occlusive disease in the rat. Hepatology 31 (2), 428–434.

Wang, Q., Spenkelink, B., Boonpawa, R., Rietjens, I.M.C.M., Beekmann, K., 2020. Use of physiologically based kinetic modeling to predict rat gut microbial metabolism of the isoflavone daidzein to S-equol and its consequences for ERα activation. Mol. Nutr. Food Res. 64 (6), 1900912.

Wang, Y.-P., Yan, J., Fu, P.P., Chou, M.W., 2005. Human liver microsomal reduction of pyrrolizidine alkaloid N-oxides to form the corresponding carcinogenic parent alkaloid. Toxicol. Lett. 155 (3), 411–420.

Widjaja, F., Wesseling, S., Rietjens, I.M.C.M., 2022. Physiologically based kinetic modelling predicts the in vivo relative potency of riddelliine N-oxide compared to riddelliine in rat to be dose dependent. Arch. Toxicol. 96 (1), 135–151.

Widjaja, F., Alhejji, Y., Yangchen, J., Wesseling, S., Rietjens, I.M.C.M., 2023. Physiologically-based kinetic modeling predicts similar in vivo relative potency of senecionine N-oxide for rat and human at realistic low exposure levels. Mol. Nutr. Food Res. 67 (4), 2200293.

Widjaja, F., Zheng, L., Wesseling, S., Rietjens, I.M.C.M., 2023. Physiologically based kinetic modeling of senecionine N-oxide in rats as a new approach methodology to define the effects of dose and endpoint used on relative potency values of pyrrolizidine alkaloid N-oxides. Front. Pharmacol. 14, 1125146.

Williams, L., Chou, M.W., Yan, J., Young, J.F., Chan, P.C., Doerge, D.R., 2002. Toxicokinetics of riddelliine, a carcinogenic pyrrolizidine alkaloid, and metabolites in rats and mice. Toxicol. Appl. Pharmacol. 182 (2), 98–104.

Wuilloud, J.C., Gratz, S.R., Gamble, B.M., Wolnik, K.A., 2004. Simultaneous analysis of hepatotoxic pyrrolizidine alkaloids and N-oxides in comfrey root by LC-ion trap mass spectrometry. Analyst 129 (2), 150–156.

Xia, Q., Zhao, Y., Von Tungeln, L.S., Doerge, D.R., Lin, G., Cai, L., et al., 2013. Pyrrolizidine alkaloid-derived DNA adducts as a common biological biomarker of pyrrolizidine alkaloid-induced tumorigenicity. Chem. Res. Toxicol. 26 (9), 1384–1396.

Xia, Q., Zhao, Y., Lin, G., Beland, F.A., Cai, L., Fu, P.P., 2016. Pyrrolizidine alkaloid-protein adducts: potential non-invasive biomarkers of pyrrolizidine alkaloid-induced liver toxicity and exposure. Chem. Res. Toxicol. 29 (8), 1282–1292.

Xiong, F., Jiang, K., Chen, Y., Ju, Z., Yang, L., Xiong, A., et al., 2020. Protein cross-linking in primary cultured mouse hepatocytes by dehydropyrrolizidine alkaloids: structure–toxicity relationship. Toxicon 186, 4–11.

Yang, X., Li, W., Sun, Y., Guo, X., Huang, W., Peng, Y., et al., 2017. Comparative study of hepatotoxicity of pyrrolizidine alkaloids retrorsine and monocrotaline. Chem. Res. Toxicol. 30 (2), 532–539.

Yang, M., Ruan, J., Fu, P.P., Lin, G., 2016. Cytotoxicity of pyrrolizidine alkaloid in human hepatic parenchymal and sinusoidal endothelial cells: firm evidence for the reactive metabolites mediated pyrrolizidine alkaloid-induced hepatotoxicity. Chem. Biol. Interact. 243, 119–126.

Yang, M., Ruan, J., Gao, H., Li, N., Ma, J., Xue, J., et al., 2017. First evidence of pyrrolizidine alkaloid N-oxide-induced hepatic sinusoidal obstruction syndrome in humans. Arch. Toxicol. 91 (12), 3913–3925.

Yang, M., Ma, J., Ruan, J., Ye, Y., Fu, P.P., Lin, G., 2019. Intestinal and hepatic biotransformation of pyrrolizidine alkaloid N-oxides to toxic pyrrolizidine alkaloids. Arch. Toxicol. 93 (8), 2197–2209.

Zhu, L., Xue, J., He, Y., Xia, Q., Fu, P.P., Lin, G., 2022. Correlation investigation between pyrrole-DNA and pyrrole-protein adducts in male ICR mice exposed to retrorsine, a hepatotoxic pyrrolizidine alkaloid. Toxins (Basel) 14 (6), 377.